# COMPARISONS OF OBSERVED SEASONAL CLIMATE FEATURES WITH A WINTER AND SUMMER NUMERICAL SIMULATION PRODUCED WITH THE GLAS GENERAL CIRCULATION MODEL

M. Halem, J. Shukla[1], Y. Mintz[2], M. L. Wu[3], R. Godbole[3], G. Herman[4], Y. Sud[5]

NASA/Goddard Space Flight Center
Laboratory for Atmospheric Sciences
Greenbelt, Maryland, USA

[1] Massachusetts Institute of Technology, Cambridge, Massachusetts, and NASA/Goddard Space Flight Center, Laboratory for Atmospheric Sciences, Greenbelt, Maryland, USA.

[2] University of California, Los Angeles, California, and NASA/Goddard Space Flight Center, Laboratory for Atmospheric Sciences, Greenbelt, Maryland, USA.

[3] National Research Council, Washington, D.C., and NASA/Goddard Space Flight Center, Laboratory for Atmospheric Sciences, Greenbelt, Maryland, USA.

[4] University of Wisconsin, Madison, Wisconsin, and NASA/Goddard Space Flight Center, Laboratory for Atmospheric Sciences, Greenbelt, Maryland, USA.

[5] Sigma Data Services Corporation, Inc., c/o NASA/Goddard Space Flight Center, Greenbelt, Maryland, USA.

## ABSTRACT

Results are presented from numerical simulations performed with the Goddard Laboratory for Atmospheric Sciences' GCM for winter and summer. The monthly mean simulated fields for each integration are compared with observed geographical distributions and zonal averages.

In general, the simulated sea level pressure and upper level geopotential height fields agree well with the observations, with the following exceptions: the winter sea level pressures are too high over the

Arctic, the Siberian high is too weak, the upper level subtropical jet
stream over Japan is not strong enough, and the mid-latitude surface
westerly winds are too weak in the Southern Hemisphere. Well simulated
features are the winter Aleutian and Icelandic lows, the summer south-
western U.S. low, the summer and winter oceanic subtropical highs in
both hemispheres, and the summer upper level Tibetan high and Atlantic
ridge. The surface and upper air wind fields in the low latitudes are
in good agreement with the observations, especially the location of the
intertropical convergence zone (ITCZ) at the earth's surface and the
anticyclonic centers of outflow in the upper air.

The geographical distributions of the earth-atmosphere radiation
balance and of the precipitation rates over the oceans are compared
with satellite observations. The patterns in both of these fields are
well simulated, but not all of the intensities of these features are
correct (for example, the observed summer negative radiation balance
over Africa appears only as a local minimum in the simulation). The
precipitation along the ITCZ is generally well simulated in the Pacific
and Indian Oceans, but is too weak in the eastern Pacific in summer and
in the Atlantic in both seasons.

The global average of the simulated absorbed solar radiation agrees
closely with satellite observations, but the globally-averaged outgoing
long wave radiation is smaller than the observed by about 10% in winter
and 20% in summer. The simulated globally-averaged planetary albedo
agrees with observations to within 10% in winter and summer.

The zonally-averaged temperatures and zonal winds are reasonably
well simulated at all levels of the troposphere in the tropics and
middle latitudes and in the lower tropospheric levels in the high lati-
tudes. In the high latitudes, the zonal mean temperatures are too cold
in the upper troposphere and stratosphere, in both seasons, and the
tropospheric jet stream is not sufficiently separated from the strato-
spheric polar night jet. The positions of the tropospheric west wind
maxima are correct, but their magnitudes are somewhat too large and in
summer the Northern Hemisphere jet is too broad. The poleward trans-
ports of momentum and sensible heat are reasonably well simulated in

the lower and middle troposphere, but there are some substantial dis-
agreements with the observed transports in the upper troposphere and
stratosphere.

The hemispherically-averaged simulated zonal and eddy available po-
tential and kinetic energies agree to within 25% with the corresponding
observed values. There is also agreement in the conversion terms, ex-
cept for the conversion of zonal kinetic to zonal available potential
energy where, in summer, the signs are in opposite direction. In agree-
ment with observation, the seasonal changes in zonal energies are smal-
ler in the Southern Hemisphere than in the Northern Hemisphere.

## 1.  Introduction

Today's General Circulation Models (GCMs) simulate reasonably well most of the observed large scale features that characterize the seasonal climate over the globe.  Still, gross deficiencies of some features can be found in almost all fields with respect to their position or intensity.  Owing to the many complex non-linear physical processes that could account for such defects, and also possible coding errors, the model at Goddard's Laboratory for Atmospheric Sciences (GLAS) is continually undergoing changes to improve its performance.  The results presented in this report were obtained with a slightly modified version of the model that was originally used for the April 1978 meeting of the JOC Study Conference of Climate Models, with minor coding errors corrected and some minor modifications to the physical parameterizations.

An important concern that emerged at the JOC Study Conference was that there are some major defects which are common to all GCMs.  The fact that these defects occur in both finite grid and spectral models with differing horizontal and vertical resolutions suggests that the cause may lie in some common error in the physical parameterizations or in the treatment of the boundary conditions.

A second area of concern identified at the conference was the need for more accurate global observations of such quantities as precipitation, diabatic heating rates and regional energy and moisture budgets, for the purpose of model diagnosis.  In this report, we present some recently acquired satellite derived distributions of radiation fluxes and ocean precipitation rates which illustrate their usefulness for evaluating the model's simulation of regional features.

Section 2 of this report gives a brief description of the current GLAS GCM and section 3 describes the initialization and imposed boundary conditions.  The results of the integration and the comparisons with observations are presented in section 4.1 for the global horizontal fields and in section 4.2 for the zonal averages and the hemispheric energetics.

## 2.  Description of the Model

The GCM that we are using at the Modeling and Simulation Facility

of GLAS was originally developed at our previous location at the Goddard Institute for Space Studies (GISS) in New York.  A description of an early version of this nine-level primitive equation model, and an evaluation of its performance in a winter season simulation, was presented by Somerville et al. (1974).  A summer simulation with essentially the same GCM, and an evaluation of its skill in simulating seasonal differences, was reported by Stone et al. (1977).  More recently, that model's simulation of the circulation over several northern hemisphere semi-arid regions was analyzed by Charney et al. (1977) in connection with his desert margin albedo feedback hypothesis.

Since the publication of those studies, modifications have been made in the model's long wave radiation parameterization, in the treatment of the surface boundary processes, and in some numerical aspects of the spatial and temporal differencing approximations.  Moreover, the integrations that are reported here were of considerably longer duration, which gave the model more time to respond to the prescribed boundary conditions.  Although the cumulative effect of these modifications on the model performance can be determined by comparison with the earlier works reported, no such comparison is made in this paper.

The modifications for the current version of the GLAS model are summarized below.

### 2.1.  *Long wave radiation*

A new parameterization for calculating the long wave radiation fluxes was developed by Kaplan and Wu (Wu, 1978).  This radiation calculation differs from the earlier version by (i) a water vapor transmittance that uses a statistical band model with the strong line version of the Curtis-Godson (Godson, 1955) approximation; (ii) inclusion of the water vapor dimer effect in the 8-13μ window region; (iii) line-by-line precalculation of $CO_2$ transmittance including fundamental bands, hot bands, and isotopes; (iv) tables of ozone transmittance calculated by Dr. N. Scott (private communication); and (v) a special treatment of the nearby layer quadrature for increased accuracy in the numerical integration.  In order to calculate the incoming long wave flux at the top, zonally-averaged climatological temperatures at 1 mb and 5 mb are prescribed.  The

dynamical response to the model to the two different formulations of long wave radiation was compared by Wu *et al.* (1978).

## 2.2. *Time step for physical processes*

The long and short wave radiation transfers were calculated at 5-hour intervals, in order to save computer time. This makes the radiation operative at every hour of the day once in every 5 days. The calculations of the other physical processes (convection, evaporation, etc.) were made at half-hour intervals.

## 2.3. *Hydrology*

The prescribed soil moisture was replaced by a prognostic soil moisture as in the UCLA model (1972), but with different formulations for the runoff, snow melt, and potential evapotranspiration, as developed by Lin *et al.* (1978).

## 2.4. *Sea surface temperature*

Monthly mean observed sea surface temperatures, provided by NCAR, were adapted to the GLAS 4° x 5° spherical grid. These temperatures were updated daily by a linear interpolation between the midpoints of two consecutive months, thereby providing smoothly varying values.

## 2.5. *Surface albedo*

Observed values of the albedo are prescribed for the land, ocean and desert regions as described by Charney *et al.* (1977). In the summer simulation, the snow albedo was calculated as a function of the snow depth, following Holloway and Manabe (1971).

## 2.6. *Grid resolution*

To overcome numerical stability problems that result from the polar convergence of the meridians and a long time-step, we introduced a variable horizontal grid with coarser spacing at the poles. The idea is similar in principle to that proposed by Kurihara (1965), but is

applied at only a few interfaces separating latitudinal bands within which the horizontal resolution is uniform. The resolution of each latitudinal band is twice that of its poleward adjacent neighbor. The Arakawa finite differencing algorithm, which applies to a spherical grid with uniform resolution, was modified to treat the non-uniform spacing at the edges separating the latitudinal subdivisions. The difference scheme was developed by Halem and Russell (1973) and maintains the quasi-conservation property of mean-square vorticity, as in the original Arakawa scheme. Although written to handle an arbitrary number of bands, the geometry used in the present model has five latitudinal bands, consisting of a central region extending from -66° to +66°, bounded by one set of bands from 70° to 78°, and a second set from 82° to 86°. The latitudinal resolution is 4° in all bands. The longitudinal resolutions are 5°, 10°, and 20°, respectively.

## 2.7. *Time step for fluid-dyanamical processes and space-averaging*

By having a coarser grid in the polar regions it was possible to increase the time step from 6 to 10 minutes. The new grid also made possible a significant reduction in the amount of horizontal averaging of the pressure gradients in the finite differencing scheme. In contrast with the increasing number of averaging operations that are applied at high latitudes with the old grid (as many as eleven complete latitudinal passes at the pole) the present version never goes above one pass near the poles. The time-alternating space-uncentered differencing scheme (TASU) of Arakawa (1972) was removed, and a high order two-gridpoint filter developed by Shapiro (1970) was applied to the potential temperature and sea level pressure. In the winter experiment this filter was also applied to the wind and moisture fields.

## 3. Specification of the Initial and Boundary Conditions for the Seasonal Integrations

Integrations were carried out for a northern hemisphere winter and a northern hemisphere summer season. Each was initialized from a real global analysis provided by the National Meteorological Center (NMC).

In all of the following, "winter" and "summer" mean the northern hemisphere winter and summer, unless the context clearly indicates otherwise.

The initial conditions for the winter simulation were valid for 00Z January 1, 1975, and the initial conditions for the summer simulation were valid for 00Z May 15, 1974. The data for the analyses were collected during the early Data Systems Tests (DST) conducted by NASA and made available to the Goddard Modeling and Simulation Facility by the Development Division of NMC.

In the winter simulation we used the Posey and Clapp (1964) regional distributions of surface albedo and snow and ice cover. In the summer simulation we used only three values of surface albedo (oceans [.07], vegetated land [.14], and deserts [.35]), in place of the Posey and Clapp data.

The winter integration was carried forward for 60 days and the summer integration for 108 days. The simulated atmospheric state variables and diabatic processes were stored at 5-hour intervals in order to sample the evolving fields at every hour of the day (once every 5 days). The simulated seasonal climates described in the following sections are based on averages, sampled with the 5-hour frequency, over the last 30 days of each integration, namely February and August.

## 4. Comparisons of Simulated and Observed Fields

The results of the winter and summer simulations are presented in two parts. First, we compare the simulated monthly mean fields with the observed ensemble means for many years. Second, we compare meridional cross-sections of the zonally-averaged atmospheric state variables and of some eddy transport quantities, for the two individual months, with the corresponding fields derived from several years of observations. We also compare the simulated and observed energy budgets for the northern hemisphere atmosphere.

### 4.1. *Global fields*

#### 4.1.1. Sea level pressure

Figure 1 shows the observed and simulated sea level pressure fields for February, and Fig. 2 shows the respective fields for August. The observed fields are from Crutcher and Davis (1969) and are based on 100 years of observations.

February. The Aleutian and Icelandic lows and the oceanic subtropical highs, in the Northern and Southern Hemispheres, are in good agreement with the observations. The position and depth of the Aleutian low is particularly good, as is the two-cell structure of the Icelandic low, although these are features which in nature show appreciable variations from year to year. The major shortcomings in the sea level pressure simulation are the excessively high pressure over the Arctic basin, the relatively weak and somewhat displaced Siberian high, and the failure to get the belt of closely spaced isobars between 40S and 60S.

August. The features which are in good agreement with observation are the highs over the subtropical oceans (which have hitherto been the most difficult feature to simulate in northern hemisphere summer), the South Asia low and its extension across North Africa, and the low over the western U.S. The major shortcomings of the simulation are that the Asian low is too deep and centered somewhat too far east, and that the pressure is too high over Antarctica.

#### 4.1.2. Geopotential heights

Figure 3 shows the observed and simulated geopotential heights of the 200 mb pressure surface for February. Figure 4 shows the respective fields for August. The observed fields are taken from Crutcher and Davis (1969).

February. The features which are reasonably well simulated are the ridge and trough located over the western and eastern coasts of North America, the ridge over the eastern Atlantic, and the strong Southern Hemisphere zonal flow. The major defect is the failure to get the tight packing of the height contours over Japan, which corresponds to the subtropical jet stream in that region.
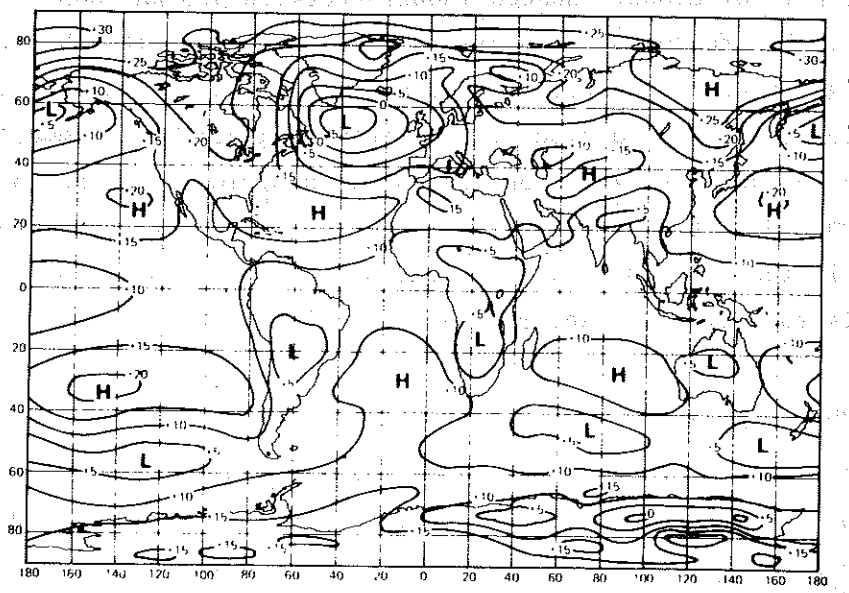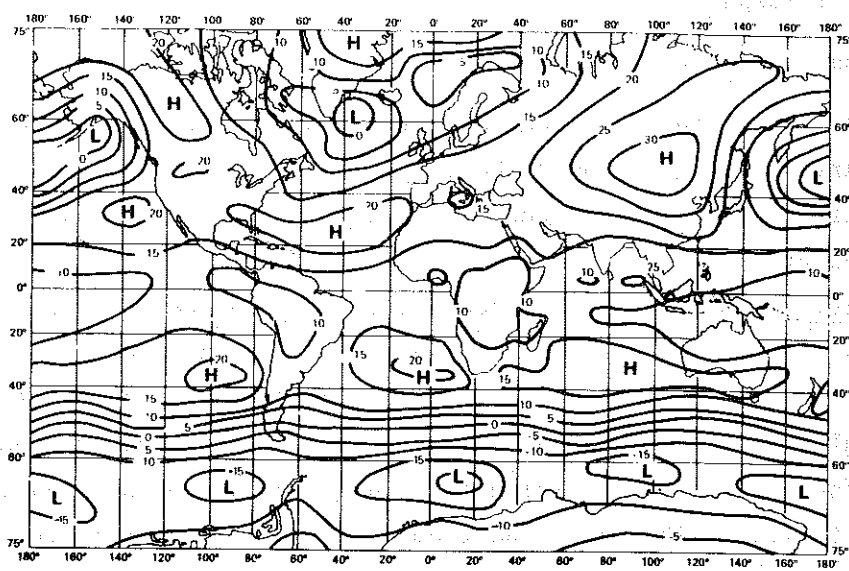
Fig. 1. Observed sea level pressure (mb - 1000) for February, after Crutcher and Davis (1969) (above); simulated sea level pressure distribution (mb - 1000) for February (below).
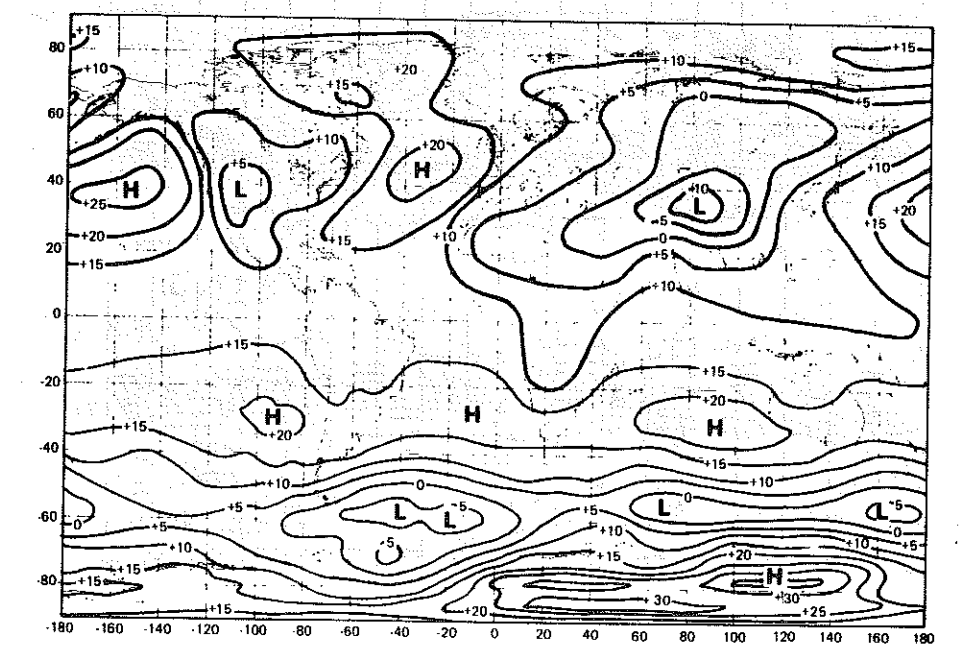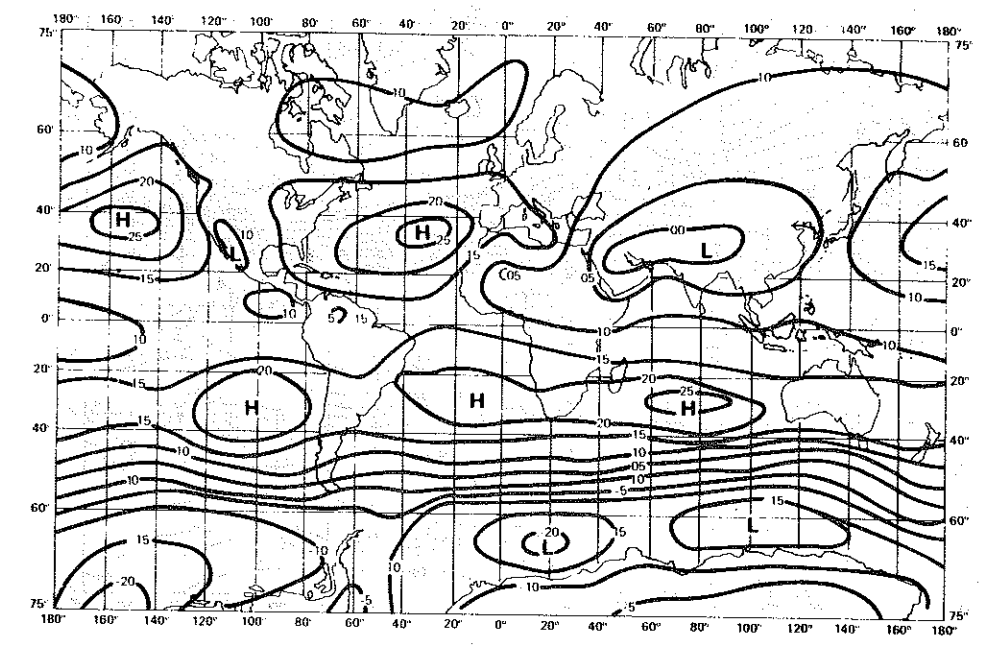


Fig. 2. Observed sea level pressure (mb - 1000) for August, after Crutcher and Davis (1969) (above); simulated sea level pressure (mb - 1000) for August (below).
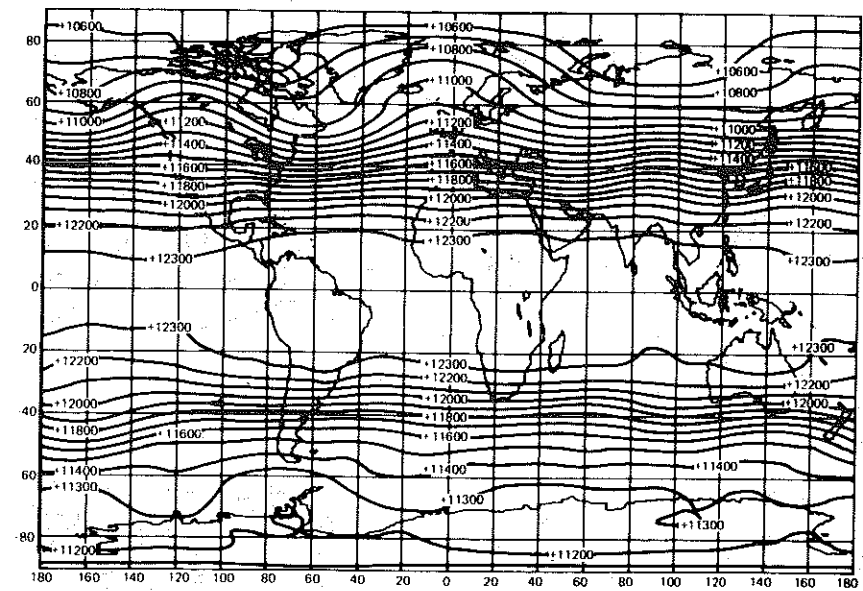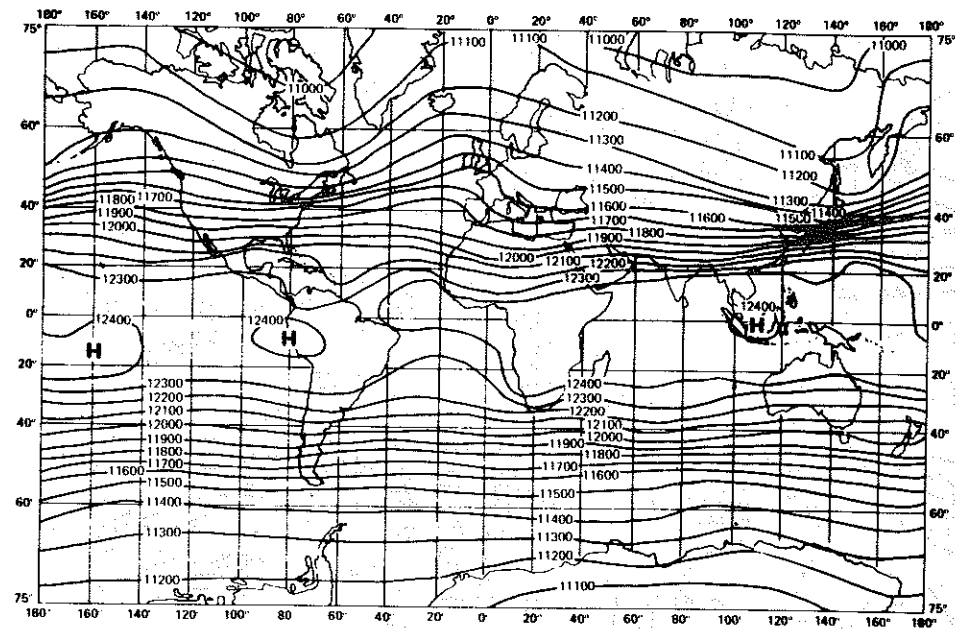
Fig. 3. Observed 200 mb geopotential height (m) for December, January, and February, after Crutcher and Davis (1969) (above); simulated 200 mb geopotential height (m) for February (below).
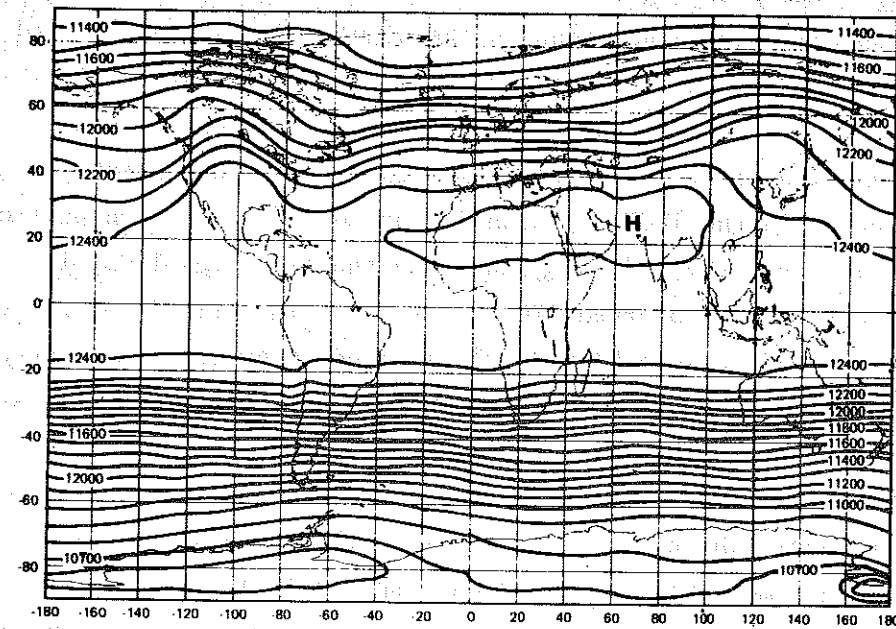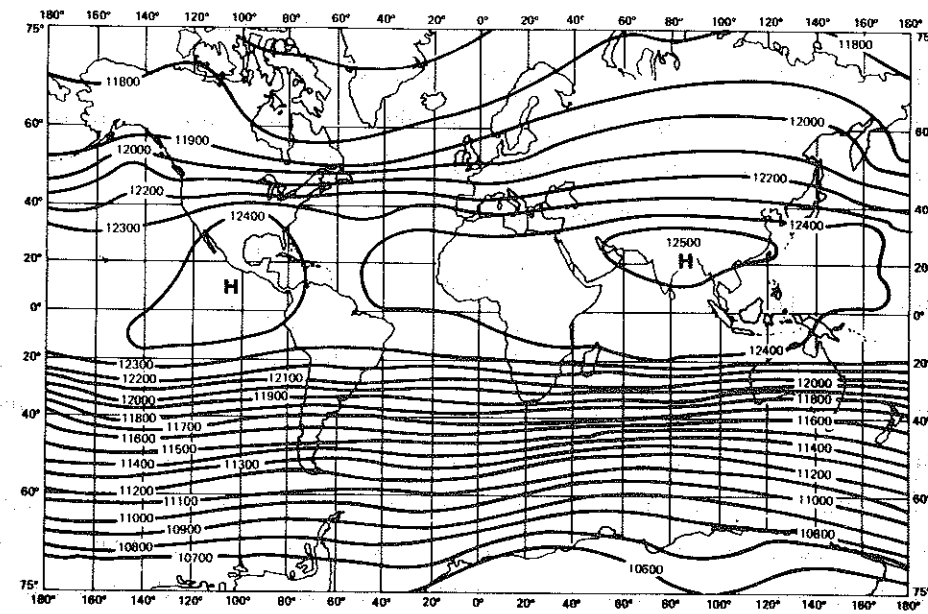


Fig. 4. Observed 200 mb geopotential height (m) for June, July, and August, after Crutcher and Davis (1969) (above); simulated 200 mb geopotential height (m) for August (below).

August. The features which are reasonably well simulated are the Tibetan high and its westward extension over North Africa, the ridge over Mexico, and the strong southern hemisphere zonal flow. The major deficiency is that the observed ridge over the Gulf of Alaska is displaced to the center of North America.

### 4.1.3. Surface winds

Figures 5 and 6 show the direction of the observed mean surface wind for January and July, and the corresponding simulated fields for February and August. The observed fields are from Mintz and Dean (1952). These direct analyses of the surface wind field, as well as their upper level counterparts, reveal the structure of the atmospheric circulation in the low latitudes much more clearly than can be inferred from the sea level and upper pressure fields.

February. There is a good correspondence between the location of the intertropical convergence zone in the simulated and the observed surface wind fields. Particularly striking is the similar way in which the ITCZ varies its position with longitude: in each case its most southerly position occurs over South America, Africa and Australia. The main discrepancy in the ITCZ location is that over the eastern part of the Pacific and over the Indian Ocean where the simulated ITCZ lies along the equator, the observed ITCZ is at about 7N latitude over the eastern Pacific and between 5° and 20°S latitude over the Indian Ocean. The flow of the surface air from the northeast and the southeast toward the ITCZ (the "trade winds") is also well simulated.

The centers and the asymptotes of anticyclonic outflow in the subtropical latitudes, which are the origins of the trade winds, are in good general agreement with observation, especially in the Southern (summer) Hemisphere; and the simulated and the observed outflow centers disagree to the extent that the simulated and observed surface pressure fields (Fig. 1) disagree. Thus, the simulation shows a separate high pressure center and a separate center of anticyclonic outflow in the western north Pacific, which the long-period averaged observed pressure and wind fields do not show. But such a double-cell structure is observed in the north Pacific in some individual years.
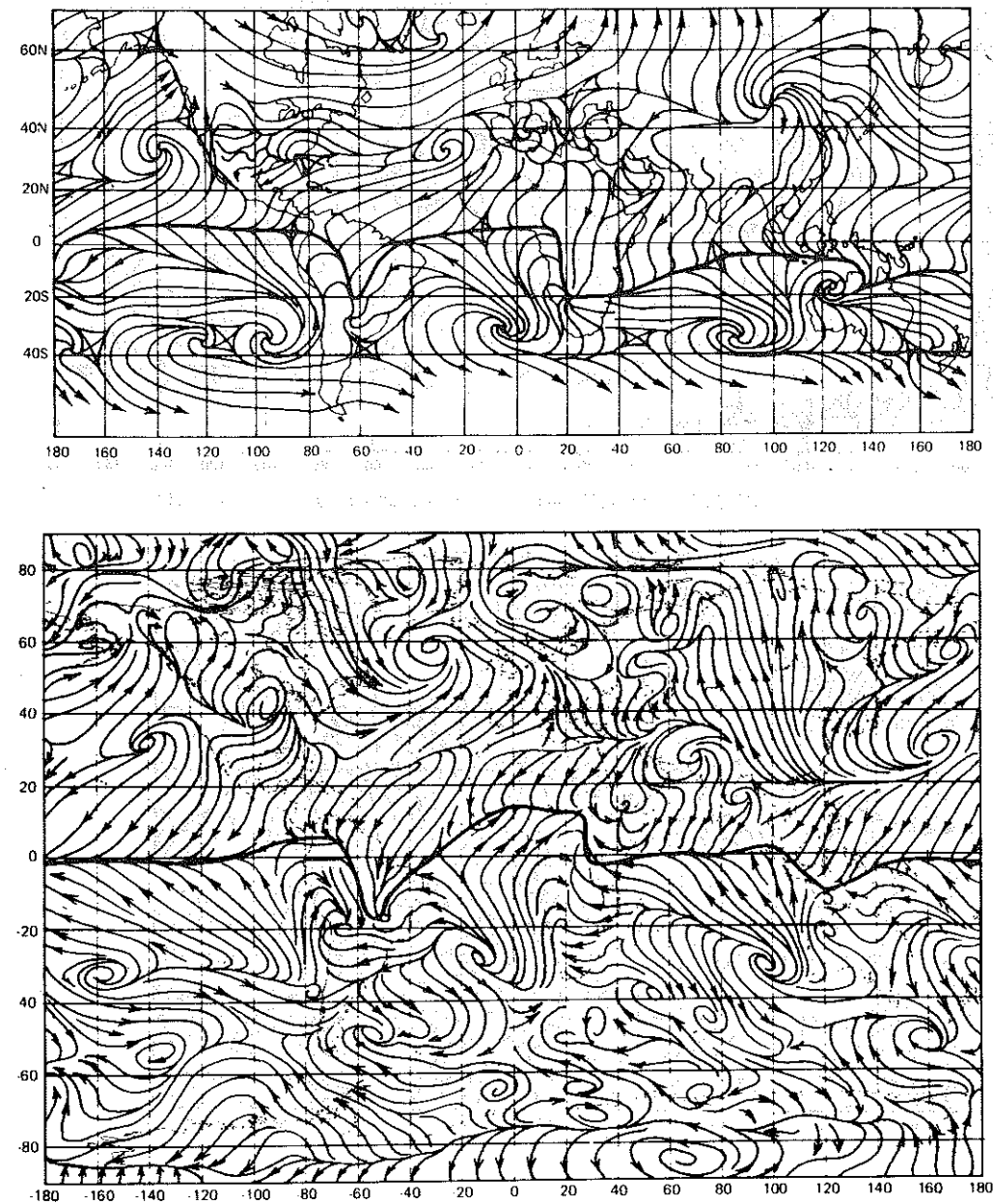
Fig. 5. Direction of the wind at the earth's surface as observed (above) for January from Mintz and Dean (1952), and as simulated for February (below).
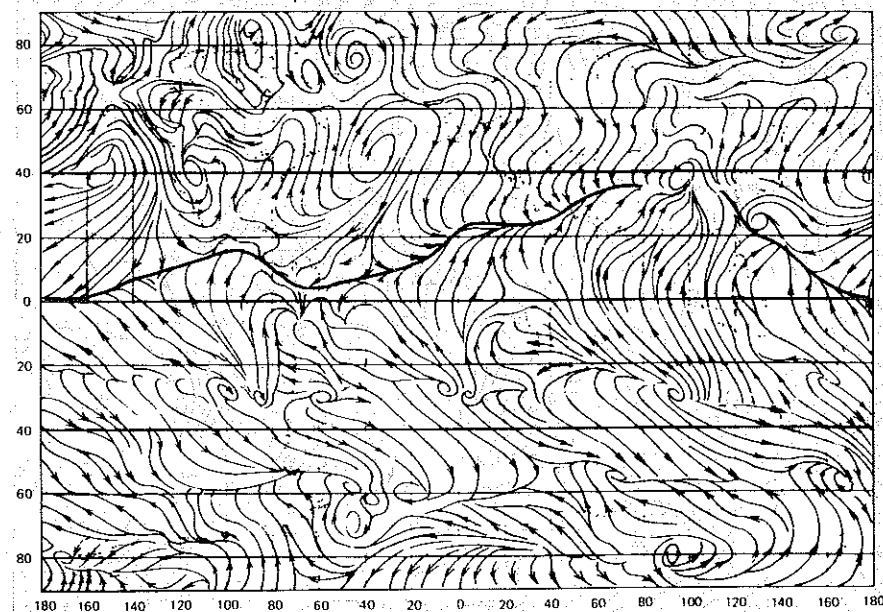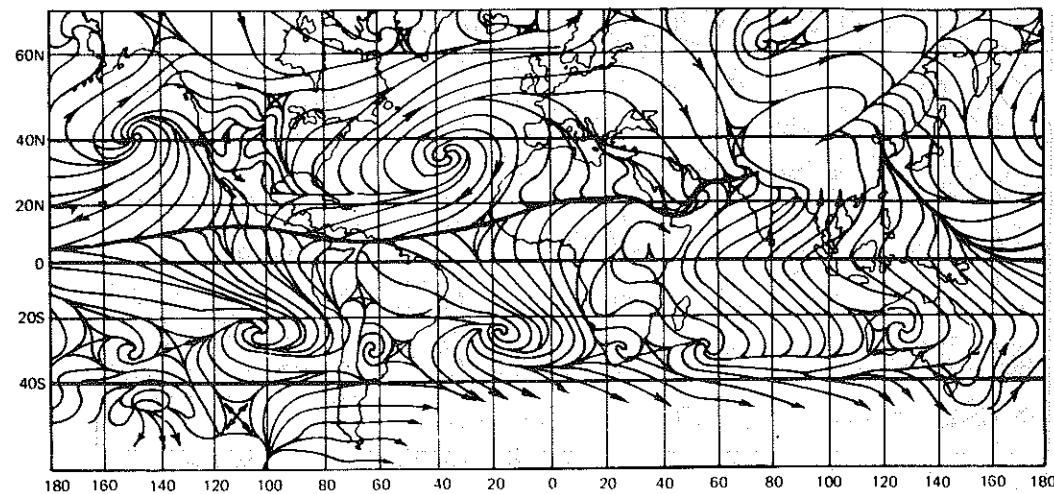
Fig. 6. Direction of the wind at the earth's surface as
observed (above) for July from Mintz and Dean
(1952), and as simulated for August (below).

August. The change in the location of the ITCZ, from February to
August, is very much alike in the observed and simulated surface wind
fields. Particularly striking is the change over South America, central
and east Africa, the Indian Ocean, south Asia, and the western Pacific.
Again it is the simulated summer hemisphere (now in the Northern Hemi-
sphere) in which the subtropical anticyclonic outflow is most clearly
defined. Over the north Indian Ocean the surface winds have correctly
changed from northeasterly to a southwesterly direction.

4.1.4. 200 mb winds

Figure 7 shows the direction of the observed and simulated mean
200 mb winds for February, and Fig. 8 shows the corresponding fields
in August. The observed fields are from Sadler (1975).

February. The simulation shows three centers of anticyclonic out-
flow in the Southern Hemisphere, at about 15S latitude, centered over
South America, Africa, and the north coast of Australia, all in agree-
ment with the observations. The observed field has a center of cyclonic
(clockwise) inflow at this latitude, just off the east coast of South
America. But in the simulation there is only a cyclonic (clockwise)
trough in this location.

In the Northern Hemisphere the simulation shows two centers of anti-
cyclonic flow at about 10N latitude over the central Atlantic and over
Africa, which are not in the observed field.

Both the simulated and observed fields show a northward cross-equa-
torial flow over South America, Africa, and Indonesia. Over the Indian
Ocean, however, the simulation does not show the well organized north-
ward cross equatorial flow that is seen in the observed field.

In the higher latitudes the wave-shaped flow pattern that is seen
in Fig. 7 coincides with the pattern of the 200 mb height field shown
in Fig. 3.

August. At this time, it is the Northern Hemisphere which shows
the well defined centers of anticyclonic outflow, both in the simulated
and observed fields. The centers over the southwestern U.S. and Tibet
are in good agreement with observation, but the simulated outflow cen-
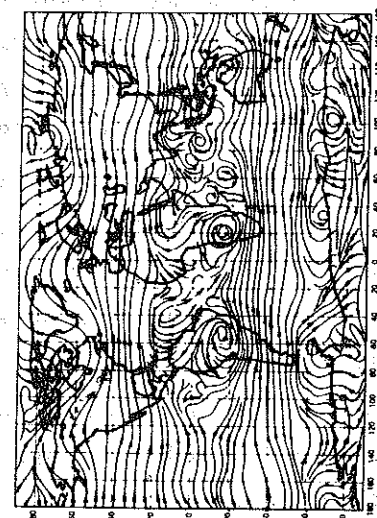ter over North Africa is not found in the observed wind field.
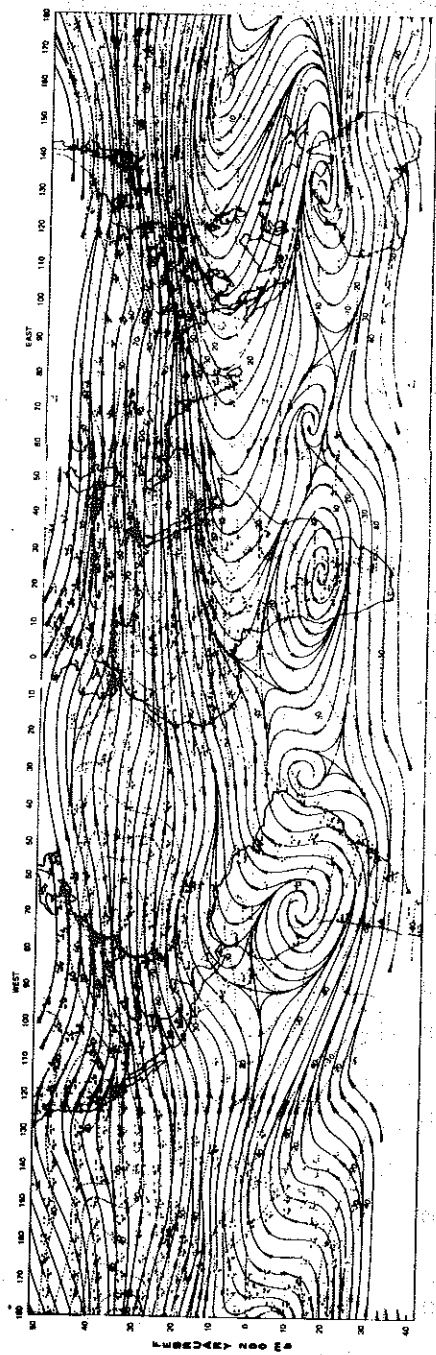
Fig. 7.  Direction of the wind at 200 mb as observed (above) from Sadler (1975), and as simulated (below) for February.
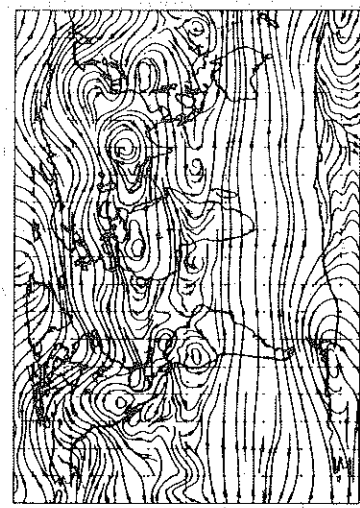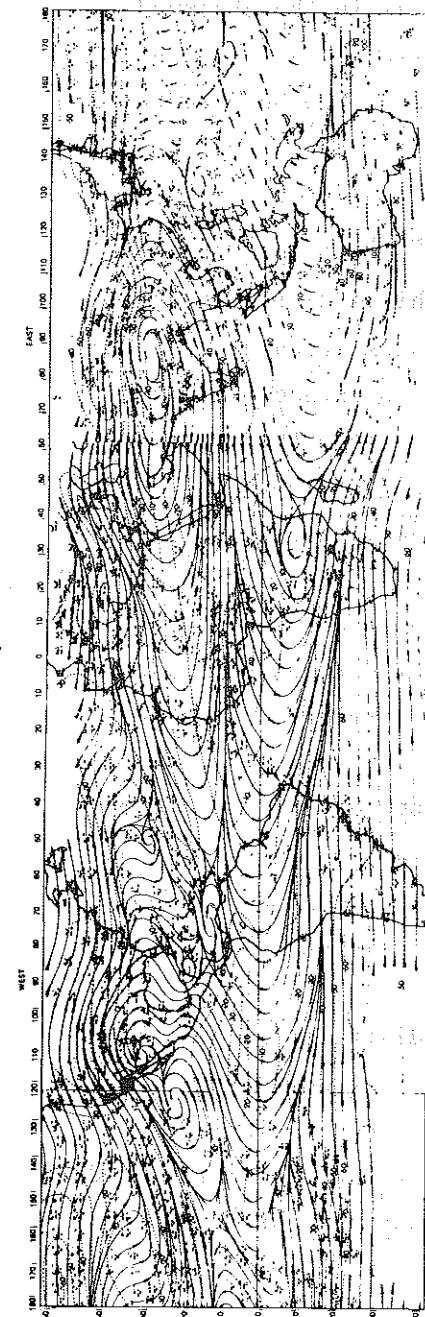


Fig. 8.  Direction of the wind at 200 mb as observed (above) from Sadler (1975), and as simulated (below) for August.

The cross-equatorial flow from the Northern to the Southern Hemisphere is not as well organized in the simulated as in the observed field, and along the equator in the eastern Pacific the simulation has a short wave in a westerly flow which is not seen in the observed wind field.

### 4.1.5. Radiation balance of the earth-atmosphere system

Global satellite observations of the geographical distribution of the radiation balance of the earth-atmosphere system are available for selected time intervals for a 10-year period. Such data can be used as diagnostic measures of the GCM's ability to simulate the prognostic variables that affect the radiation balance, namely, temperature, cloudiness, water vapor distribution and surface reflectively.

Table 1 describes the radiative properties of the clouds in the GLAS model. The short wave radiation parameterization recognized eight types of model clouds to which it assigns the optical properties indicated in Table 1. The long wave radiation parameterization treats all of the clouds as "black".

Figures 9 and 10 show the net radiation balance derived from Nimbus-3 satellite observations for the last 2 weeks in January 1970 and the last 2 weeks in July 1969, and the simulated radiation balances for February and August. (The solar declination angle changes by 8° in the second half of January and 10° in February.)

February. The features of the geographical distribution of the net monthly radiation balance that the model simulates reasonably well are the centers of maximum heating over the oceans in the low-latitudes of the Southern Hemisphere and the relative minima over South America and southern Africa. A major difference with observation, however, is the position of the line of zero heating, which in the simulation is about 5° to 10° too far north.

August. The model simulates the northward shift of the lines of zero heating and the latitude of maximum heating. Especially noteworthy is the fact that the model produces a minimum of summertime radiational heating over north Africa, so that the horizontal Laplacian of heating (and hence its effect on the horizontal circulation) is the

Table 1. Radiative properties of clouds in the GLAS model.

| Cloud type | Layers (1) | Analogy | Optical thickness | Albedo |
|---|---|---|---|---|
| Supersaturation | 2 | Ci | 1 | .12 |
| Supersaturation | 3 | Ci | 2 | .21 |
| Supersaturation | 4 | As | 4 | .34 |
| Supersaturation | 5 or 6 | As | 6 | .44 |
| Supersaturation | 7 or 8 or 9 | St | 8 | .51 |
| Penetrating convection | 4-7 or 5-8 or 6-9 | Cb | 32 | .81 |
| Mid-level convection | 5 or 6 | Ac | 8 | .51 |
| Low-level convection | 7 or 8 | Cu | 16 | .68 |

For long wave heating rates, all clouds are "black."

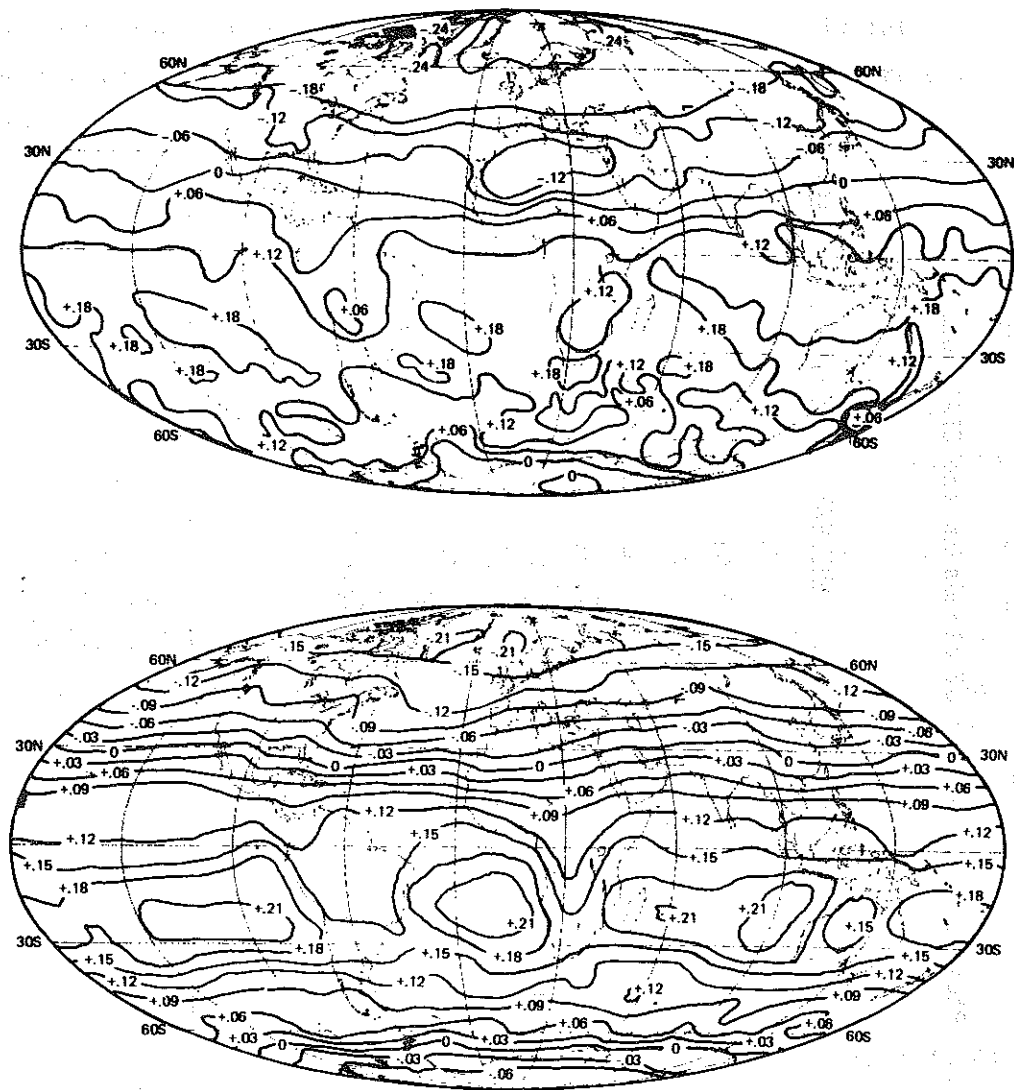(1) Layers are ~110 mb thick and layer one corresponds to interval between 10 mb and 120 mb.

Fig. 9. Radiation balance (cal cm$^{-2}$min$^{-1}$) of the earth-
atmosphere system as observed (above) during the
period January 21 to February 3, 1970 from Raschke
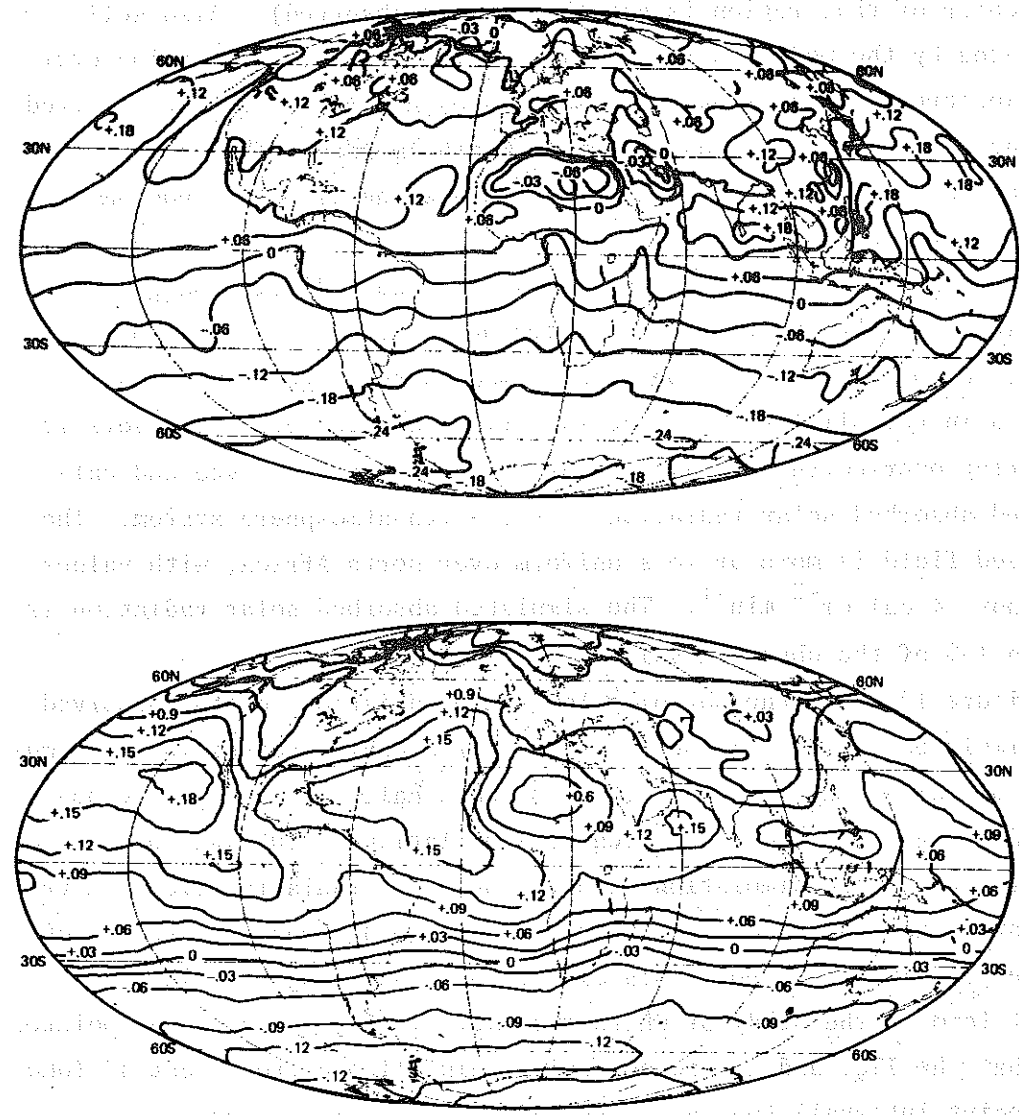*et al.* (1973), and as simulated (below) for February.



Fig. 10. Radiation balance (cal cm$^{-2}$min$^{-1}$) of the earth-
atmosphere system as observed (above) during the
period July 16 to 31, 1969 from Raschke *et al.*
(1973), and as simulated (below) for August.

same as in the observed field (even though the sign of the heating at
the center of that region is not the same as observed). Also well
simulated by the model is the minimum of the radiational heating over
northwestern North America. The model does not reproduce the observed
heating minimum off the west coast of North America. This may be due
to the fact that the model does not simulate the planetary boundary
layer stratus clouds.

The separate components associated with the radiative budget cal-
culations for the summer are presented here because they show how
satellite observations can be used by models to diagnose the possible
defects in the simulation of the radiation balance (e.g., the deficit
occurring over north Africa). Figure 11 shows the observed and cal-
culated absorbed solar radiation of the earth-atmosphere system. The
observed field is more or less uniform over north Africa, with values
of about .4 cal $cm^{-2}$ $min^{-1}$. The simulated absorbed solar radiation is
within 15% of the observed values.

Figure 12 shows the outgoing long wave radiation for the observed
and simulated fields. We see that the meridional gradient in the simu-
lated outgoing long wave radiation is about half as large as the ob-
served along a belt across Africa between latitudes 10° and 20°N. Thus,
comparisons of the simulation with the observed radiative fields have
suggested that the gradient structure of outgoing long wave radiation
is the principal problem. This discrepancy was recognized in a dif-
ferent form in the study of Charney *et al.* (1977), where it was pointed
out that the ITCZ and its accompanying rainfall occurred about 4° (one
grid point interval) too far north in the model simulation.

### 4.1.6. Global radiation budget

Table 2 compares the observed and simulated globally-averaged net
radiation balance and its separate components, for February and August,
and also shows the respective mean monthly planetary albedos. The ob-
served fields are from Raschke *et al.* (1973). We see that the simu-
lated albedo is about 10% higher than the observed. The incoming solar
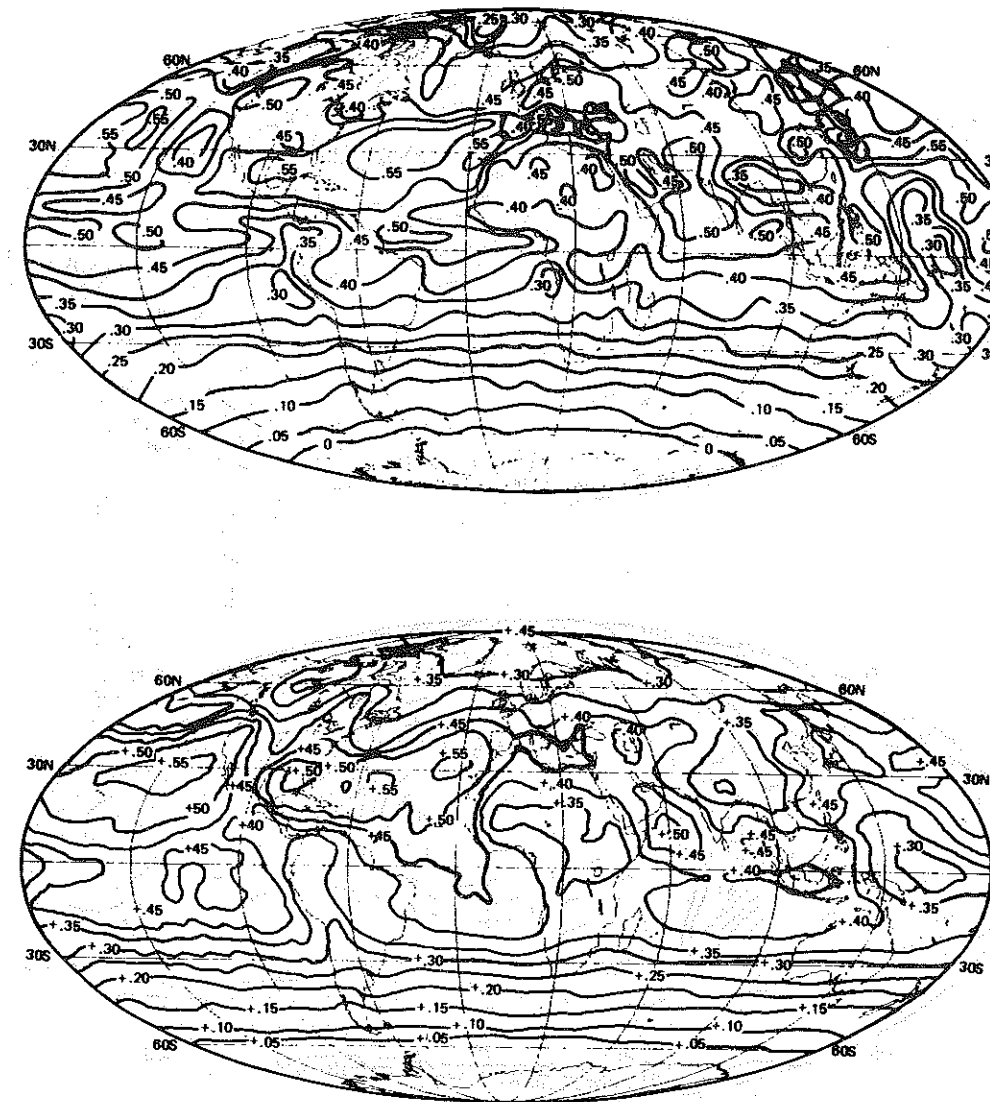radiation differences are small and are probably mainly the result of

Fig. 11. Solar radiation (cal $cm^{-2}min^{-1}$) absorbed in the earth-
atmosphere system as observed (above) during the period
July 16 to 31, 1969 from Raschke *et al.* (1973), and as
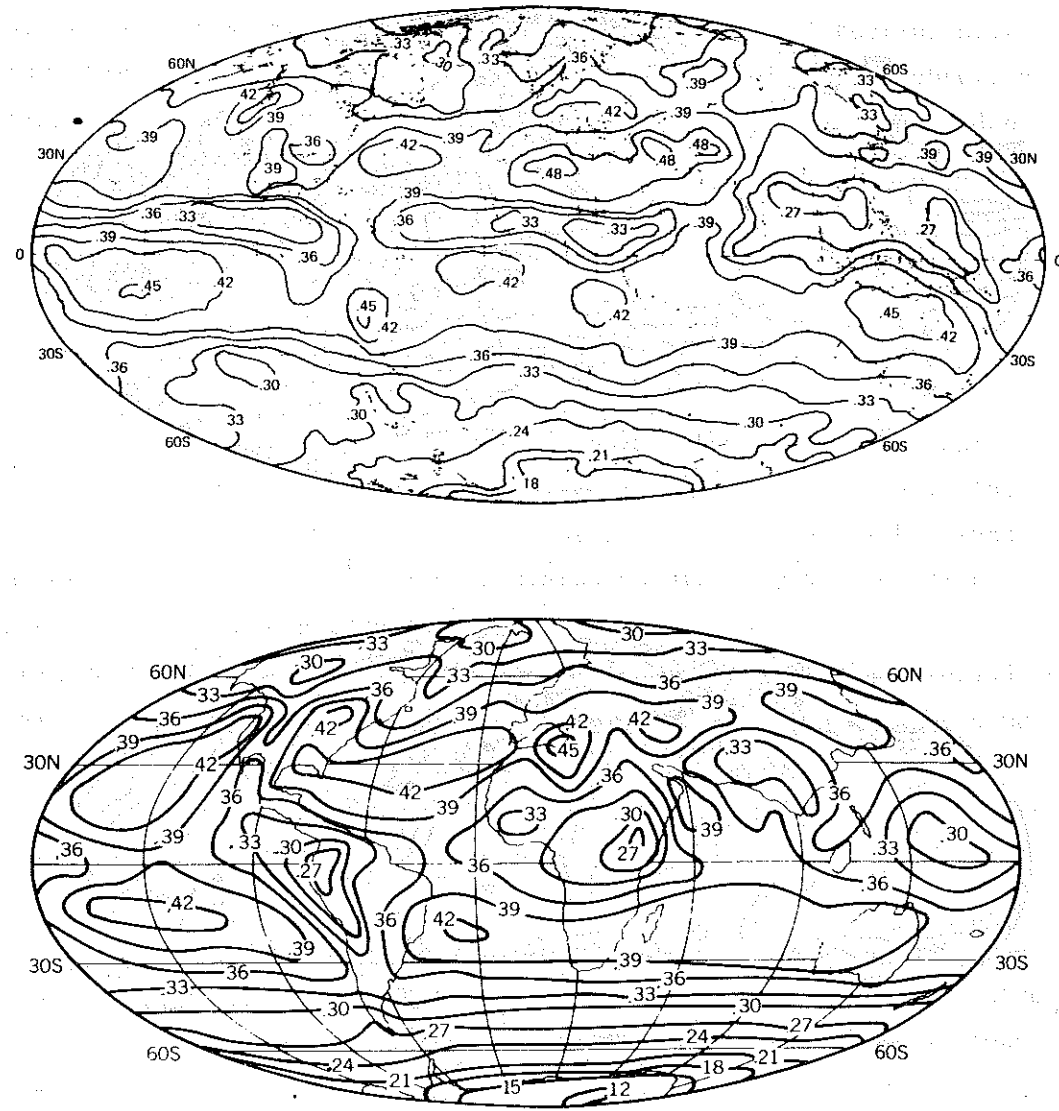simulated (below) for August.

Fig. 12. Outgoing radiation (cal cm$^{-2}$min$^{-1}$) emitted from the earth-atmosphere system to space as observed (above) during the period July 16 to 31, 1969 from Raschke *et al.* (1973), and as simulated (below) for August.

Table 2. Global radiation budget of the earth-atmosphere system (cal cm$^{-2}$ min$^{-1}$).

| | Solar radiation | | | Long wave radiation | Net |
|---|---|---|---|---|---|
| | Incoming | Absorbed | Albedo | Outgoing | Radiation balance |
| Observed (Jan. 21 through Feb. 3, 1970) | .501 | .361 | .283 | .337 | .024 |
| Simulated (February) | .513 | .356 | .305 | .295 | .061 |
| Observed (July 16 through July 31, 1969) | .472 | .339 | .281 | .354 | -.015 |
| Simulated (August) | .488 | .334 | .315 | .294 | .040 |

using a solar constant of 1.95 cal $cm^{-2}$ $min^{-1}$ for the observations and 2.0 cal $cm^{-2}$ $min^{-1}$ for the model simulation.

The simulated absorbed solar radiation shown in Table 2 is in close agreement with observation, accounting for the good agreement in the planetary albedo. Table 2 shows that the simulated outgoing long wave radiation is about 12% less in winter and 17% less in summer than observed. As a result, the net radiation balance is higher in the simulation by .037 cal $cm^{-2}$ $min^{-1}$ in winter and .055 cal $cm^{-2}$ $min^{-1}$ in summer. Several reasons may be responsible for this. First, clouds are assumed to be uniformly black to long wave radiation over the entire grid area (400 x 400 km and 100 mb) regardless of the type of clouds. Second, the model generates excessive high level cloud cover in the equatorial regions, contributing not only to a higher albedo but also lowering the outgoing long wave radiation; the outgoing long wave radiation responds more strongly to an overestimate of high level clouds than does the short wave radiation.

Although the net radiation balance is positive in both seasons, the global mean temperatures of the simulation are constant to within 0.2%. From Table 3 we see that the net imbalance at the surface of the earth-atmosphere system is comparable with the imbalance of radiation at the top of the atmosphere as shown in Table 2. The storage in the atmosphere and over land is negligible in both seasons (not shown in Table 3). This implies that the oceans with their prescribed temperatures, and the melting of permanent sea-ice, can act as a sink in the model to absorb the excess radiation balance calculated at the top of the atmosphere.

## 4.1.7. Global precipitation

Observations of the geographical distribution of rainfall over the oceans were recently acquired from the microwave instrument ESMR on the Nimbus-5 satellite. A rainfall atlas derived from these data has been prepared by Rao *et al.* (1976) with 4° x 5° resolution. Figure 13 shows the observed and model-simulated fields of rainfall for February and Fig. 14 shows the respective fields for August.

Table 3. Heat balance at surface of the earth (cal $cm^{-2}$ $min^{-1}$).

| | Net flux incoming solar radiation at surface | Net flux upward long wave radiation at surface | Net flux upward sensible heat flux | Net atmospheric heating by condensation(1) | Net surface balance |
|---|---|---|---|---|---|
| February | .278 | .078 | .040 | .101 | .059 |
| August | .251 | .073 | .048 | .094 | .036 |

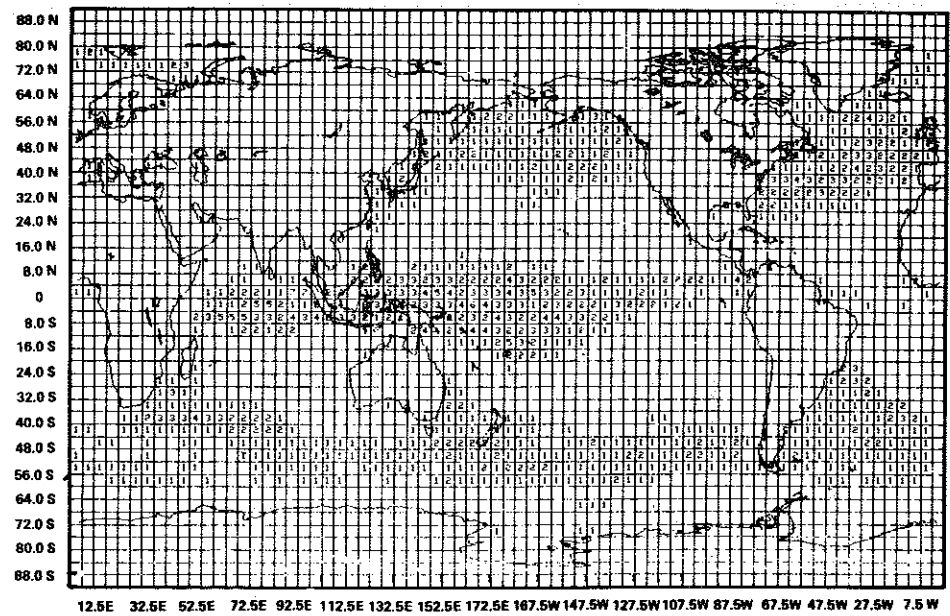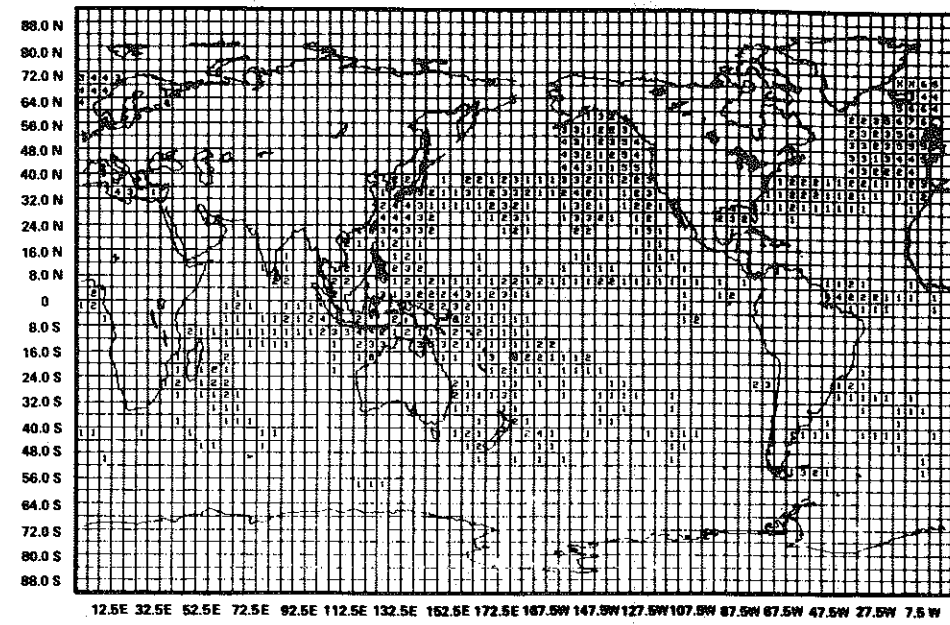(1) This is approximated by net evaporation.

Fig. 13. Oceanic rainfall rate (.1 mm/hr) as ESMR-derived (above) from Rao *et al*. (1976) for February 1975, and as simulated (below) for February.
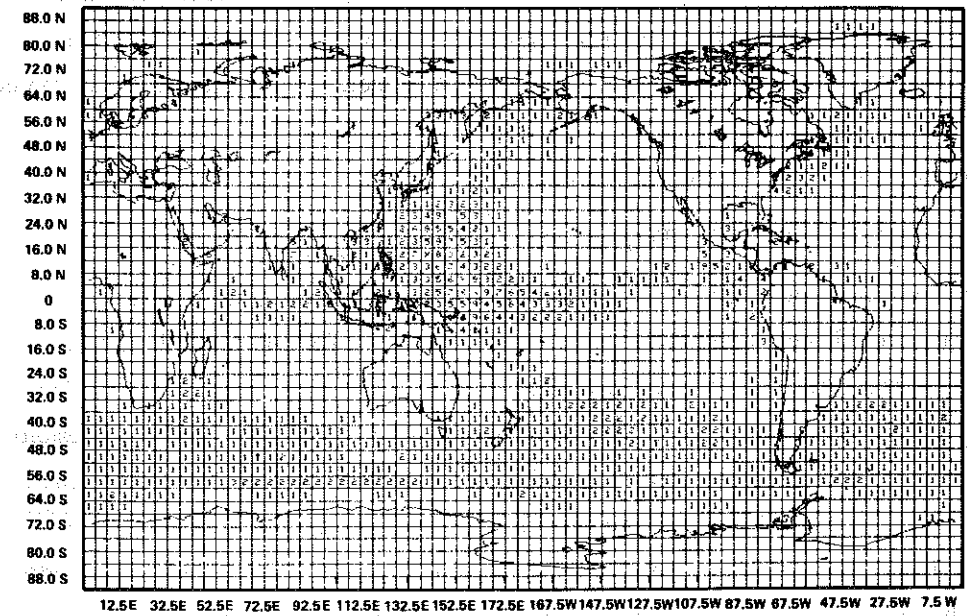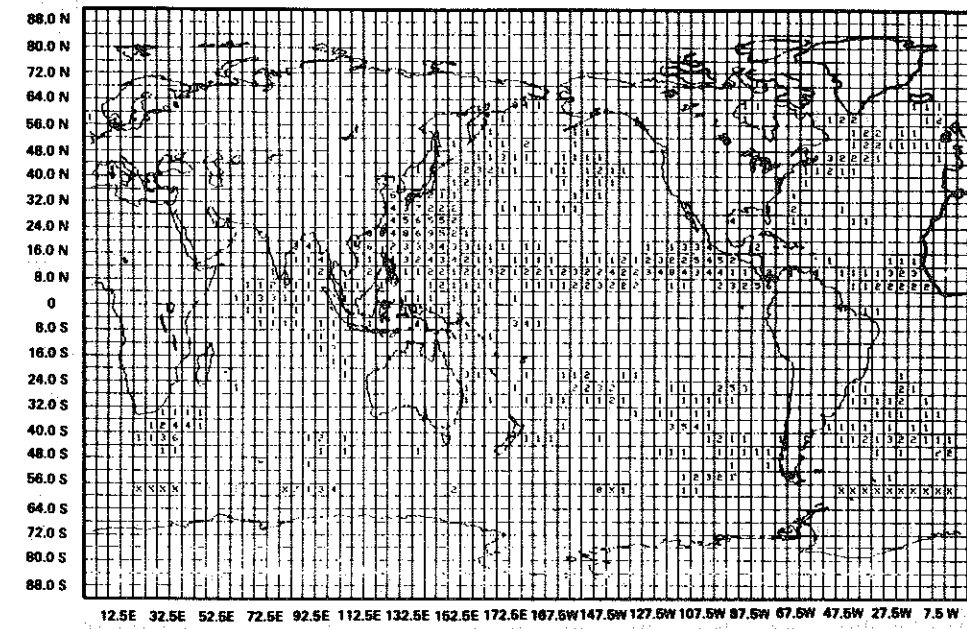


Fig. 14. Oceanic rainfall rate (.1 mm/hr) as ESMR-derived (above) from Rao *et al*. (1976) for August 1974, and as simulated (below) for August.

February. The general features of the monthly mean rainfall over
the oceans are well simulated by the model. The simulated field shows
the bands of precipitation along the ITCZ in the Pacific and the Indian
Ocean, although somewhat too far south in the central Pacific. The
model, however, is deficient in its simulation of the Atlantic ITCZ
rainfall. Over the North Pacific, North Atlantic, tropical Indian
Ocean, and middle latitude southern hemisphere oceans, the simulation
shows larger precipitation rates than the observations.

August. The general features of the simulated fields that agree
well with observations are the equatorial band of precipitation across
the Pacific, the precipitation in the Bay of Bengal, and the intense
precipitation over the tropical and subtropical western North Pacific,
although the simulated amounts are too large. Again the model failed
to produce any significant precipitation along the Atlantic ITCZ. An-
other discrepancy is that the model produced a band of precipitation
oriented NW-SE over the ocean east of Australia, which does not show
in the observations. The model produced a band of rainfall over all
of the middle latitude southern hemisphere oceans that was not observed.

## 4.2. Cross-sections of zonally-averaged fields

### 4.2.1. Temperatures and zonal winds

Superimposed in Figs. 15 and 16 are the observed and simulated
zonally-averaged temperatures and zonal winds. The observed fields
are taken from Newell et al. (1972).

February. The zonally-averaged temperatures are in good agreement
with observations in the lower to mid-troposphere and low to mid-lati-
tudes. The simulated temperatures in the upper troposphere in the
equatorial regions also agree well with observation both in magnitude
and in the intensity of the meridional gradients which extend out
toward mid-latitudes. The apparent temperature differences in the
vicinity of the equatorial tropopause are largely due to the linear
interpolation used in the contouring routine for the purpose of obtain-
ing values at 100 mb from model values at 65 mb and 175 mb.

The principal deficiency is that the upper level polar temperatures
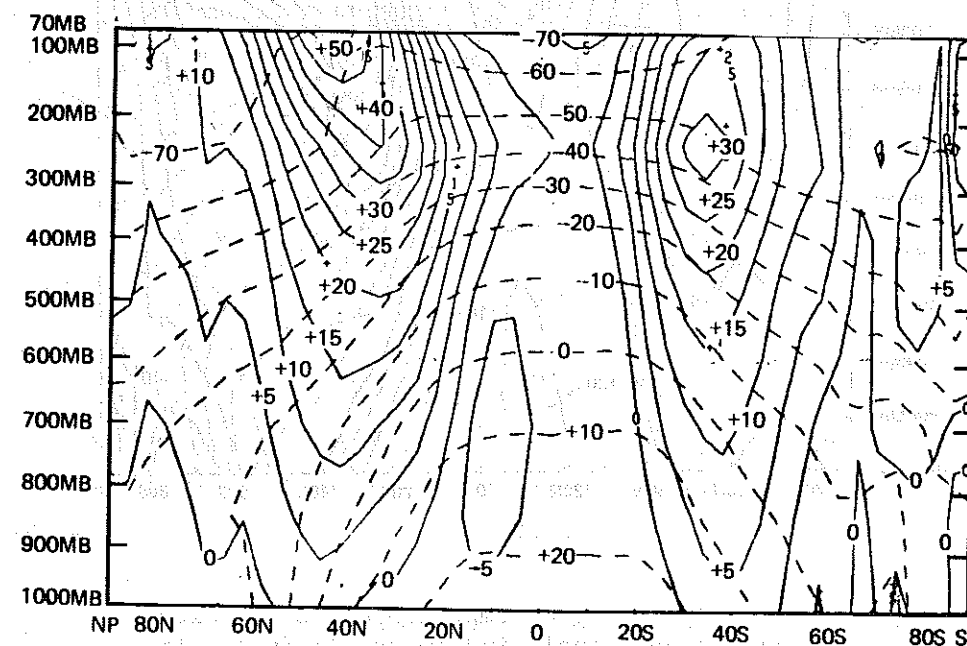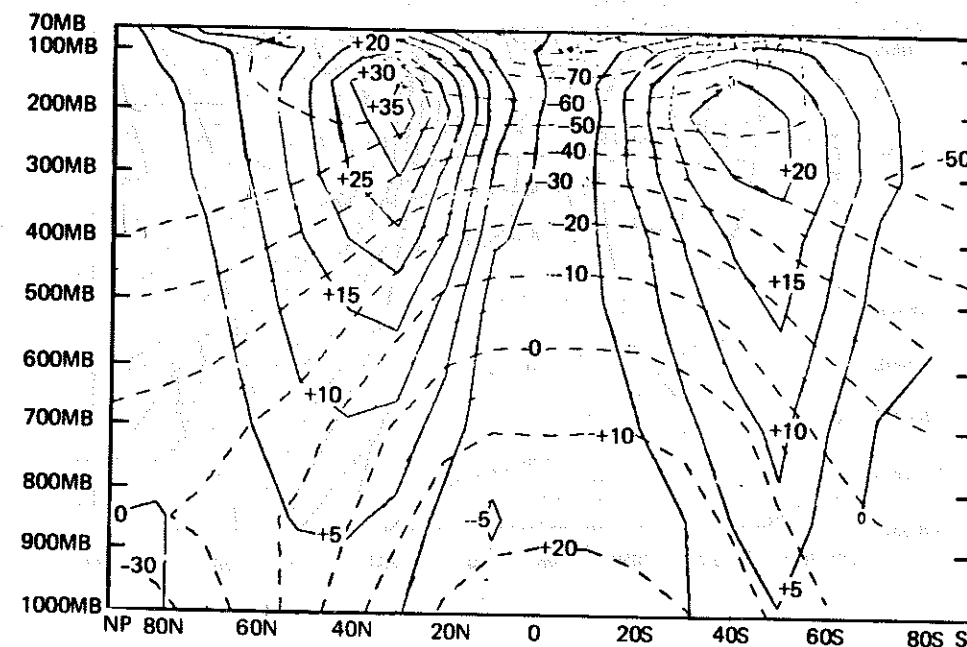are too cold by 10° to 20°C, and that the observed upper level zones

Fig. 15. Zonally-averaged temperature (°C) (broken lines) and
zonal wind (m sec⁻¹) (solid lines) as observed (above)
for December, January and February from Newell et al.
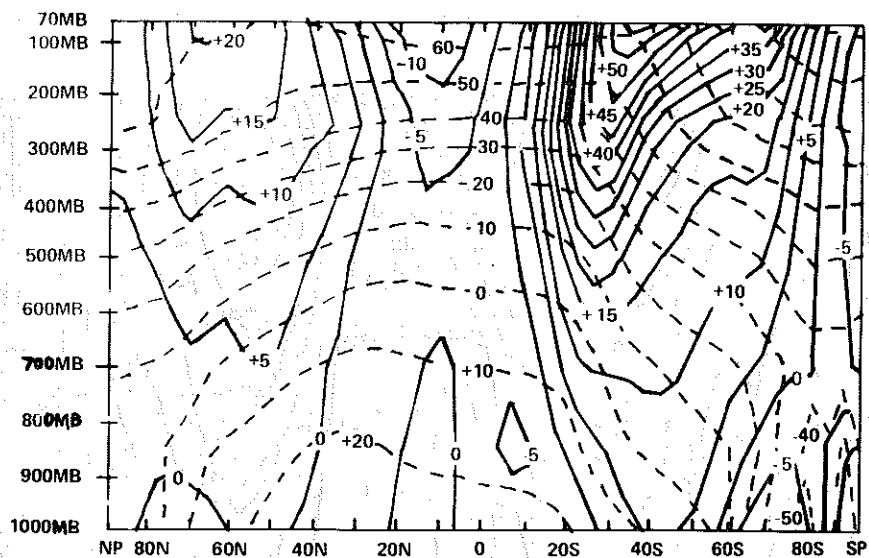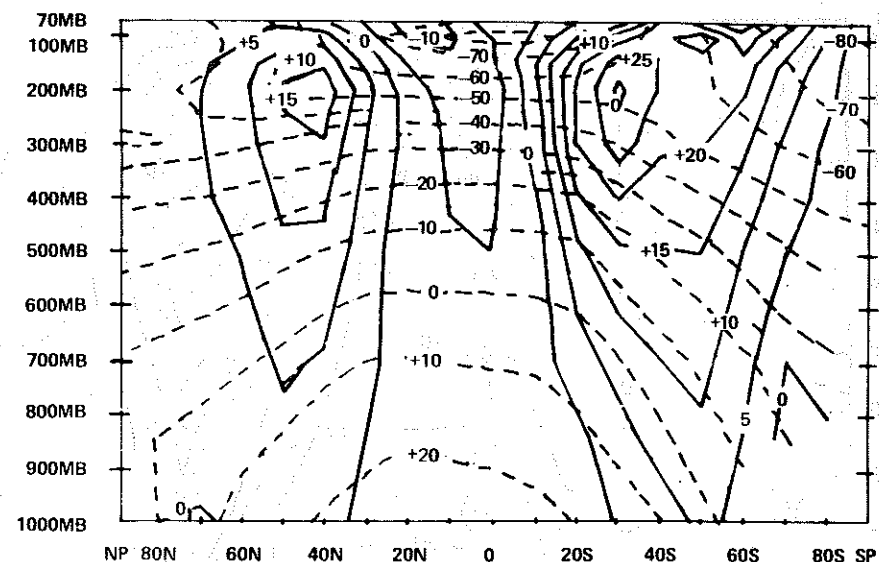(1972), and as simulated (below) for February.

Fig. 16. Zonally-averaged temperature (°C) (broken lines) and zonal wind (m sec$^{-1}$) (solid lines) as observed for June, July and August from Newell *et al.* (1972), and as simulated (below) for August.

of warmest air at about 50° latitude are missing. This appears to be a common defect in all the GCM simulations presented at this conference. It is not yet known what the cause of this error is, but possible explanations have attributed this defect to insufficient poleward eddy heat transports, artificial boundary conditions at the top of the model atmosphere, unrealistic cloudiness in the polar regions, or unrealistic simulation of orographically forced waves. Further discussion of this problem is offered in a separate section below.

The simulated zonal wind is generally in good agreement with the observed wind wherever the temperature is well simulated, and not in agreement where the simulated temperature is not correct. Thus, the low-latitude easterlies and mid-latitude westerlies in both hemispheres are well simulated but the simulation does not have a stratospheric polar night westerly jet stream that is separated from the tropospheric westerly jet stream, and produces westerly jets whose magnitudes are too large.

August. The zonally-averaged temperatures shown in Fig. 16 are in good agreement in the lower and middle troposphere, but the upper level temperatures in the high latitudes are again excessively cold (by 10° to 20°C). The westerly zonal winds are reasonably well simulated in the lower and middle troposphere, but are much too strong in the upper troposphere and stratosphere. The tropical easterlies are well simulated in both extent and magnitude.

4.2.2. Meridional transport of momentum by eddies

February. Figure 17 shows the observed northward transport of westerly momentum by standing and transient eddies, for December, January and February (Newell *et al.*, 1972), and the simulated transport for February. In the Northern Hemisphere, the maximum northward transport in the simulation is in the vicinity of the westerly west wind maximum, in agreement with observation. The simulated maximum, however, does not decrease rapidly at the higher levels as is observed. In the Southern Hemisphere the subtropical poleward transport is weaker than the observed. In both hemispheres the high latitude
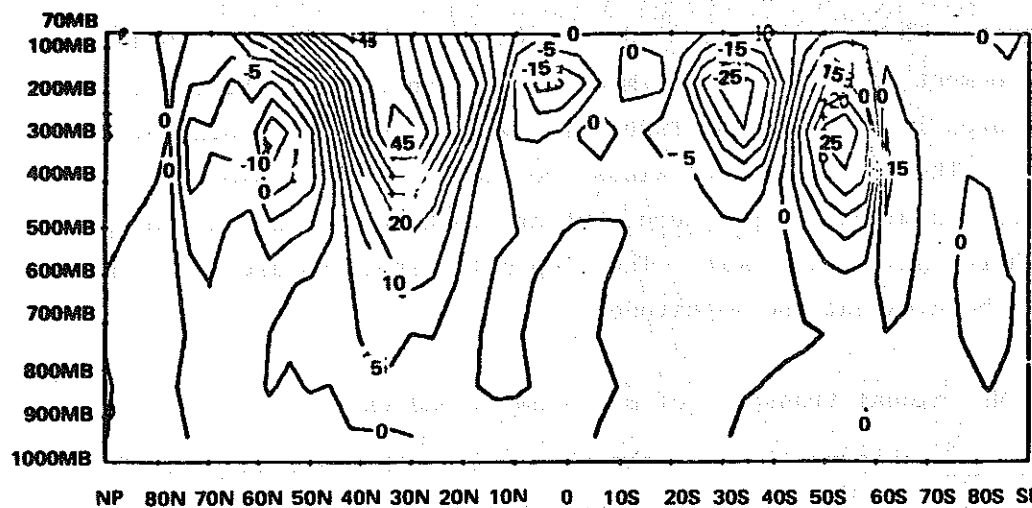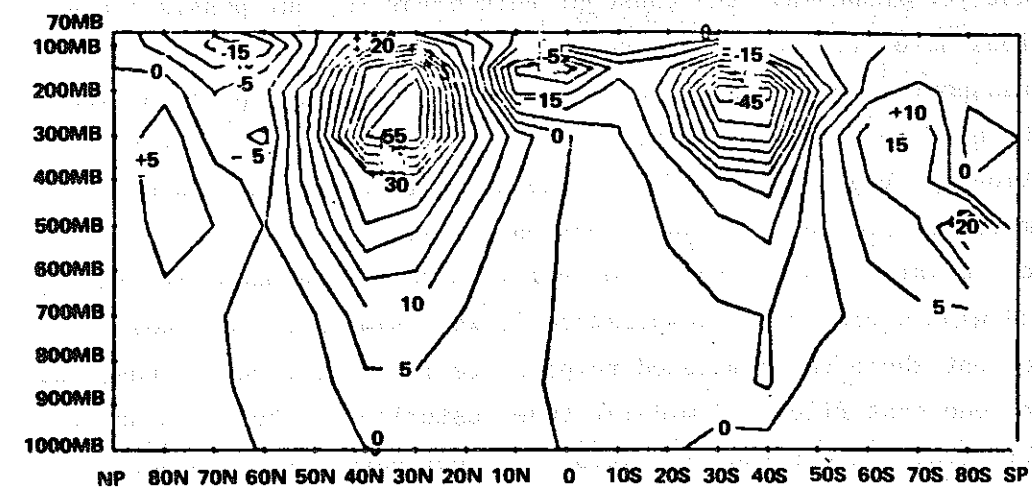
Fig. 17.  Northward transport of westerly momentum by eddies
(m$^2$ sec$^{-2}$) as observed (above) for December, January
and February from Newell *et al.* (1972), and as simu-
lated (below) for February.

equatorward transports are stronger than observed and extend too far
from the poles.  The high level cross-equatorial westerly momentum
transport, from the winter to the summer hemisphere, has the correct
pattern and sign but is somewhat too weak.

August.  The observed northward eddy momentum transport for June,
July and August (Newell *et al.*, 1972) is shown in Fig. 18.  The model-
produced transport for August is also shown in Fig. 18.  The simulated
transports agree reasonably well with observations, as does the loca-
tion, sign and intensity of the upper level cross-equatorial flow.  But
again, in both hemispheres, the model produces subpolar equatorward
westerly momentum transports that are larger than observed and occur
too far from the poles.

### 4.2.3.  Meridional transport of sensible heat by eddies

The observed northward flux of sensible heat by standing and trans-
ient eddies for the three winter months and the three summer months
are shown in Figs. 19 and 20, respectively (Newell *et al.*, 1972).  The
corresponding simulated fluxes for February and August are also shown
in Figs. 19 and 20.

February.  The simulated eddy heat transport has the same general
distribution as the observed, except that the lower level maxima are
closer to the ground.  The upper level maxima are also somewhat weaker
and farther from the poles than the observed, so that the magnitude of
the upper level heat flux convergence is somewhat smaller than the ob-
served in both hemispheres.

August.  Again, the general pattern of the simulation is correct,
but with some important differences.  In the summer, the simulation
appears to have somewhat stronger poleward heat transport than observed.
A conspicuous deficiency is that between 50° and 80°S latitude where
the observed upper level eddy heat transport is toward the pole, the
simulated heat transport is away from the pole.

### 4.2.4.  The problem of the cold upper tropospheric temperatures at high latitudes

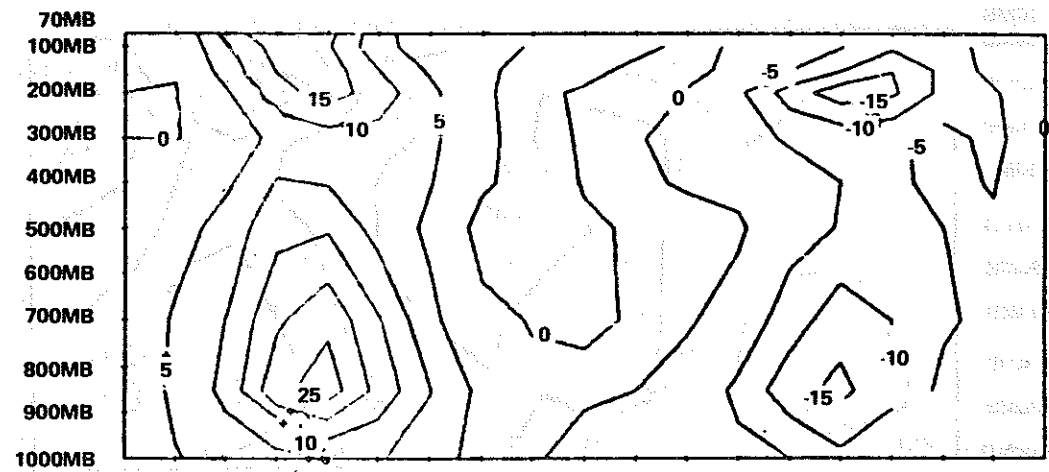The failure of the GCMs, as reported at this JOC meeting, to simulate
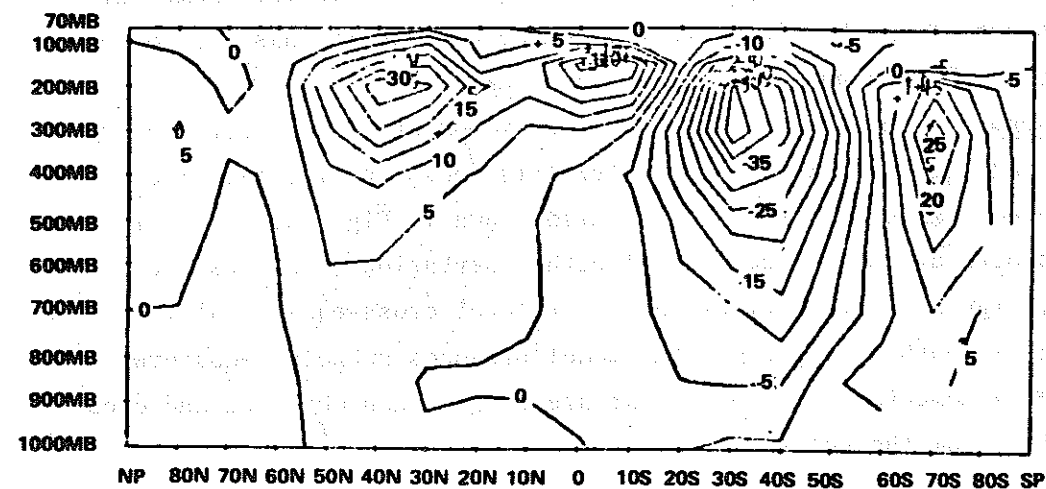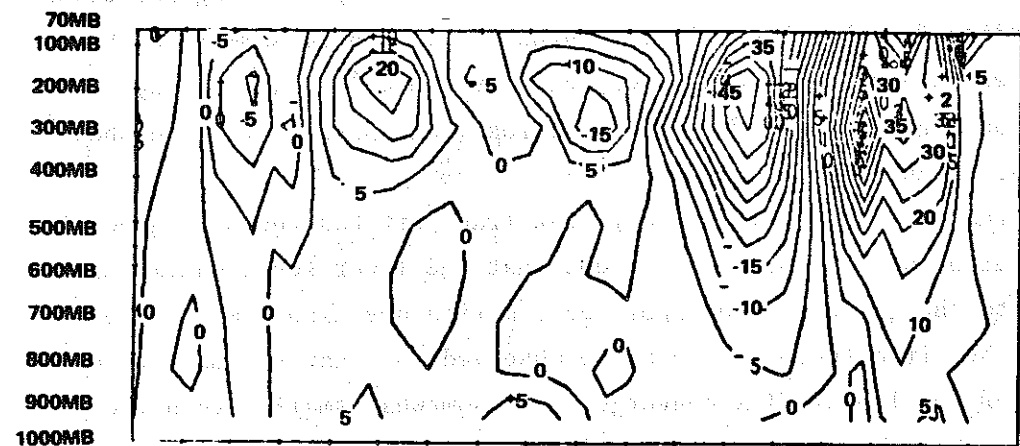
Fig. 18.  Northward transport of westerly momentum by eddies
(m² sec⁻¹) as observed (above) for June, July and
August from Newell *et al*. (1972), and as simulated
(below) for August.
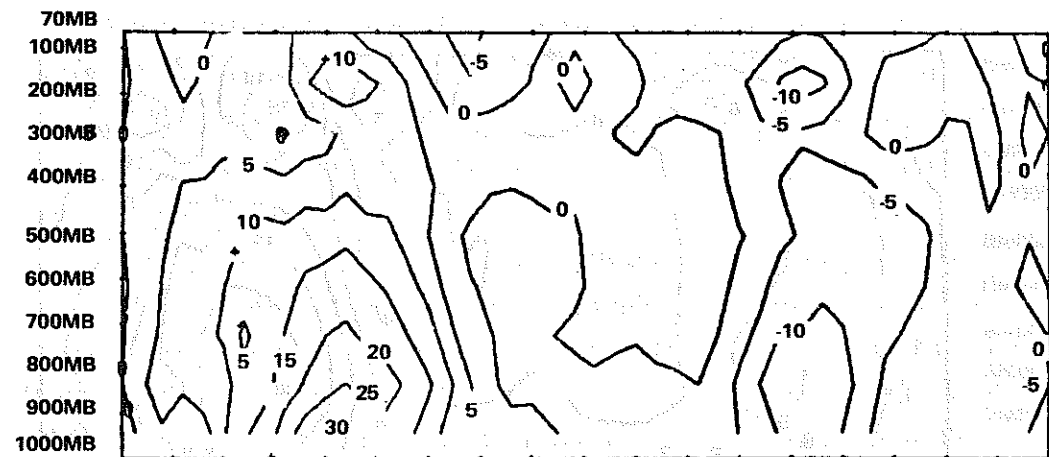


Fig. 19.  Northward transport of sensible heat by eddies
(deg m sec⁻¹) as observed (above) for December,
January and February from Newell *et al*. (1972),
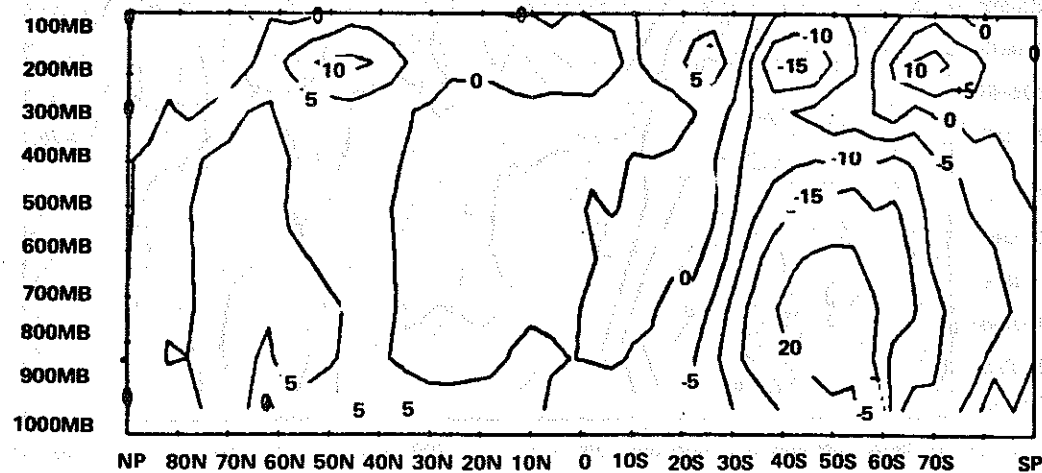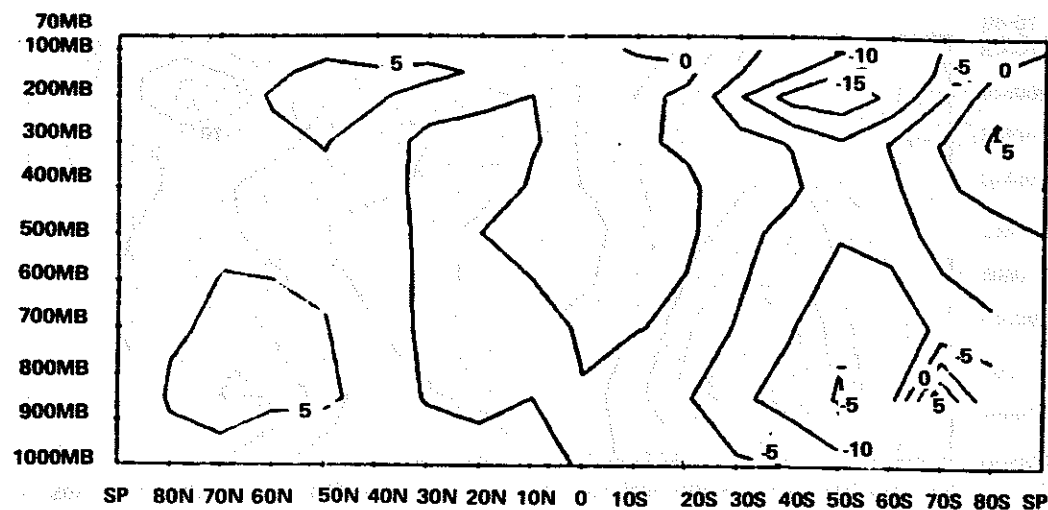and as simulated (below) for February.

Fig. 20. Northward transport of sensible heat by eddies
(deg m sec$^{-1}$) as observed (above) for June, July
and August from Newell *et al.* (1972), and as
simulated (below) for August.

the polar climate raises serious questions on their applicability for realistic climate sensitivity experiments. It is important that this problem be recognized and additional studies be carried out to examine the implications of this deficiency in interpretating the results of various sensitivity and predictability studies. At this point it is not even clear whether this deficiency is caused by inadequate numerical treatment of the thermal and dynamical responses of the atmosphere, the formulation of the upper and lower boundary conditions, or inadequacy of the parameterization of physical processes. The similar behavior of widely varying models suggests a common cause and several possible explanations are mentioned below.

Stone *et al.* (1977) have suggested that the cold arctic temperatures in winter are caused by an inadequate simulation of the Aleutian and Icelandic lows. This deficiency is associated with the underestimate of the zonal meridional heat transport primarily in wave number three. They assert this underestimate is mainly due to the deficiency in the poleward eddy flux of sensible heat as indicated in the previous section. While they find this to be a principal factor in the winter, the summer cold temperatures they attribute to deficiencies in the radiation, both solar and terrestrial.

Arakawa (personal communication) has suggested that existing models may be deficient in the simulation of orographically forced waves and their fluctuations, not just becuase of excessive smoothing of the surface topography--a smoothing that has partly been introduced to avoid computational noise, but rather their failure to produce the correct dynamical response to steep and high mountains. He claims that the dynamical influence on the upper level polar temperature does not depend solely on the magnitude of the poleward eddy heat transport, but that it depends on the difference between the poleward eddy heat transport and the equatorward transport by the mean meridional circulation, which cancel for linear neutral waves but do not cancel for non-linear fluctuating waves. He believes that by maintaining conservation of potential enstrophy in the numerical advection scheme, the simulation of planetary waves and lee cyclogenesis would be greatly improved.

Lindzen *et al.* (1968) have suggested that there may be an effect from an imposed upper lid in the model atmosphere which for thermally forced perturbations produces spurious oscillations. It is likely that such artificially generated perturbations may affect the dynamical heat fluxes. In particular, Eliassen and Palm (1961) have shown that it is possible for downward propagating waves in the westerlies to transport heat equatorward.

These are only tentative explanations and more detailed model diagnostic studies and theoretical studies are needed to understand this behavior of the GCMs.
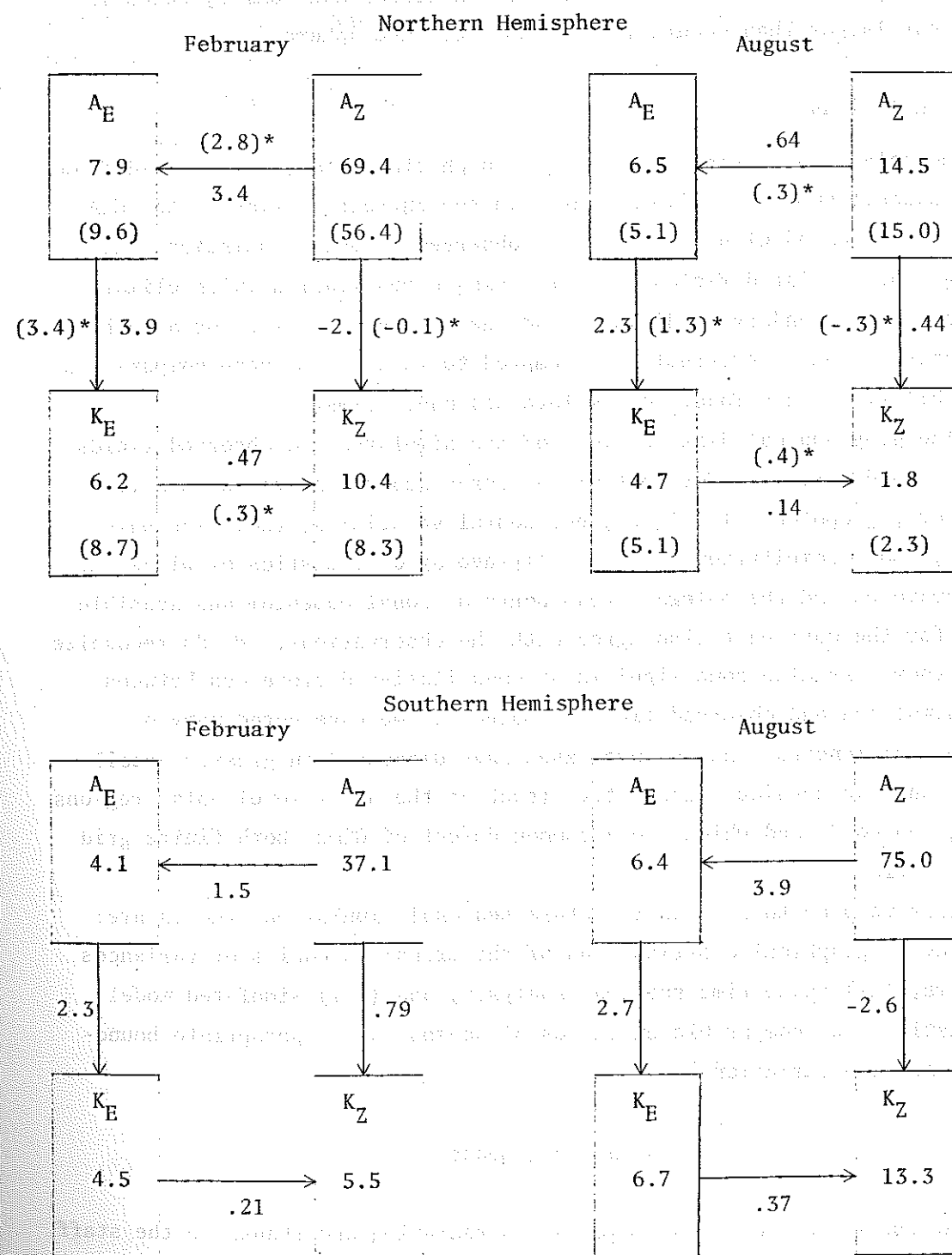
### 4.2.5. Energy cycle

Table 4 shows the integrated energies and energy transformations for February and August in the two hemispheres. The figures in parentheses are the observed values as estimated by Peixoto and Oort (1974).

February. The simulated zonal available potential and kinetic energies in the Northern Hemisphere are about 25% higher than observed while the corresponding eddy energies are about 25% lower. The conversion terms are within 20% of Peixoto and Oort's estimates, except for the conversion between zonal available potential and zonal kinetic energies for which the model conversion is about an order of magnitude larger than observed.

August. The agreement in the simulated energetics is good, and is consistent with the climate change from winter to summer. The zonal potential energy for summer is of the same magnitude as the observed while the zonal kinetic energy is 20% weaker than observed. Eddy kinetic and eddy available potential energy are within 10% of observed values. The conversion from zonal kinetic to zonal available potential energy in the simulation shows a significant reduction from winter to summer and is in the opposite direction of Peixoto and Oort's estimate. The remaining conversion terms in the simulations are in general agreement with their observed estimates. The zonal kinetic and zonal available potential energies for the summer Southern Hemisphere are substantially larger than the summer northern hemispheric energies, but the

Table 4. Simulated Energy Cycle



Northern Hemisphere

February — August

$A_E$ 7.9 (9.6) ← (2.8)* / 3.4 — $A_Z$ 69.4 (56.4)

$A_E$ 6.5 (5.1) ← .64 / (.3)* — $A_Z$ 14.5 (15.0)

(3.4)* 3.9 ↓ $A_E \to K_E$ ; -2. (-0.1)* ↓ $A_Z \to K_Z$

2.3 (1.3)* ↓ ; (-.3)* .44 ↓

$K_E$ 6.2 (8.7) → .47 / (.3)* → $K_Z$ 10.4 (8.3)

$K_E$ 4.7 (5.1) → (.4)* / .14 → $K_Z$ 1.8 (2.3)

Southern Hemisphere

February — August

$A_E$ 4.1 ← 37.1 / 1.5 — $A_Z$ 37.1

$A_E$ 6.4 ← 3.9 — $A_Z$ 75.0

2.3 ↓ ; .79 ↓

2.7 ↓ ; -2.6 ↓

$K_E$ 4.5 → .21 → $K_Z$ 5.5

$K_E$ 6.7 → .37 → $K_Z$ 13.3

* These conversion terms are taken for January and July from Oort and Peixoto (1974).

change from winter to summer is not as great. The southern hemisphere
eddy energies show a 35% variation between winter and summer, which is
somewhat larger than occurs for the Northern Hemisphere.

## 5. Conclusions

Monthly mean statistics of some atmospheric fields, as obtained from
two seasonal numerical simulations with the current version of the GLAS
GCM, are compared with corresponding observed climate statistics. Al-
though the simulated fields are for a single realization (with climato-
logical mean boundary conditions) and the observations are for a number
of years, we have nevertheless attempted to infer from these comparisons
the ability of this model to simulate seasonal climate.

The geographical distributions of the simulated and observed fields
are in good agreement for most of the large-scale features of sea level
pressure, geopotential heights, horizontal velocities, radiation bal-
ances, and precipitation. The zonally-averaged statistics of winds and
temperatures and the poleward transports of zonal momentum and sensible
heat for the most part also agree with the observations. We do recognize
that there are also some significant quantitative differences between
the simulated and observed fields. Moreover, we have noted many of
these deficiencies, and in some cases have discussed in greater detail
those that we consider substantive (such as the upper level polar regions
being too cold) and which are a common defect of GCMs, both finite grid
and spectral.

What we plan to address to future seasonal simulation studies are:
(i) the geographical distributions of the transient eddies or variances
in time, (ii) space-time spectral analyses, and (iii) simulated model
statistics over comparable ensembles of seasons with appropriate bound-
ary condition variations.

REFERENCES

Arakawa, A., 1972: Design of the UCLA atmospheric general circulation model. Tech. Rept. No. 7, Department of Meteorology, University of California, Los Angeles, California.

Charney, J. G., W. J. Quirk, S. H. Chow and J. Kornfield, 1977: A comparative study of the effects of albedo change on drought in semi-arid regions. *J. Atmos. Sci., 34*, 1366-1385.

Crutcher, H. L., and O. M. Davis, 1969: U.S. Navy Marine Climatic Atlas of the World. NAVAIR 50-1C-54, Naval Weather Service Command, Washington, D.C.

Eliassen, A., and E. Palm, 1961: On the transfer of energy in stationary mountain waves. *Geofysiske Publikasjoner, 22*, 23 pp.

Godson, W. L., 1955: The computation of infrared transmission by atmospheric water vapor. *J. Meteorol., 12*, 272-284.

Halem, M., and G. Russell, 1973: A split-grid differencing scheme for the GISS model. *Research Review, 1973* (Part 2, applications), Goddard Institute for Space Studies, GSFC/NASA, Greenbelt, Maryland.

Holloway, J. L., and S. Manabe, 1971: Simulation of climate by a global general circulation model. 1. Hydrologic cycle and heat balance. *Mon. Wea. Rev., 99*, 335-370.

Kurihara, Y., 1965: Numerical integration of the primitive equations on a spherical grid. *Mon. Wea. Rev., 93*, 399-415.

Lin, J. D., J. Alfano and P. Bock, 1978: A space-documentation of a ground hydrology parameterization used in the GISS atmospheric GCM. Tech. Rept., University of Connecticut, Storrs, Connecticut.

Lindzen, R. S., E. S. Batten and J.-W. Kim, 1968: Oscillations in atmospheres with tops. *Mon. Wea. Rev., 96*, 133-140.

Mintz, Y., and G. Dean, 1952: The observed mean field of motion of the atmosphere. *Geophys. Res. Papers, 17*, 1-65.

Newell, R. E., J. M. Kidson, D. G. Vincent and G. J. Boer, 1972: *The General Circulation of the Atmosphere and Interactions with Extratropical Latitudes*, Vols. 1 and 2, MIT Press, Cambridge, Massachusetts.

Oort, A. H., and J. P. Peixoto, 1974: The annual cycle of the energetics of the atmosphere on a planetary scale. *J. Geophys. Res., 79*, 2705-2719.

Peixoto, J. P., and A. H. Oort, 1974: The annual distribution of atmospheric energy on a planetary scale. *J. Geophys. Res., 79*, 2149-2159.

Posey, J. W., and P. F. Clapp, 1964: Global distribution of normal surface albedo. *Geofisica International, 4*, 33-48.

Rao, M. S. V., W. V. Abbot III and J. S. Theon, 1976: Satellite-derived global oceanic rainfall atlas (1973 and 1974), NASA SP-410, NASA, Washington, D.C.

Raschke, E., T. H. Vonder Haar, M. Pasternak and W. R. Bandeen, 1973: The radiation balance of the earth-atmosphere system from Nimbus-3 radiation measurements. NASA TN D-7249, NASA, Washington, D.C.

Sadler, J. C., 1975: The upper tropospheric circulation over the global tropics. Department of Meteorology, University of Miami, Miami, Florida.

Shapiro, R., 1970: Smoothing, filtering and boundary effects. *Rev. Geophys. Space Phys., 8*, 359-387.

Somerville, R. C. J., P. H. Stone, M. Halem, J. E. Hansen, J. S. Hogan, L. M. Druyan, G. Russell, A. A. Lacis, W. J. Quirk and J. Tenenbaum, 1974: The GISS model of the global atmosphere. *J. Atmos. Sci., 31*, 84-117.

Stone, P. H., S. Chow and W. J. Quirk, 1977: The July climate and a comparison of the January and July climates simulated by the GISS general circulation model. *Mon. Wea. Rev., 105*, 170-194.

Wu, M. L., 1978: Infrared energy exhange in the atmosphere. NASA Goddard Space Flight Center, Greenbelt, MD (unpublished manuscript). Submitted for publication to *J. Atmos. Sci.*

Wu, M. L., L. D. Kaplan and R. Godbole, 1978: Influence of systematic radiation differences on the dynamics of a model atmosphere. Third Conference on Atmospheric Radiation, American Meteorological Society, June 28-30, 1978, Davis, California.